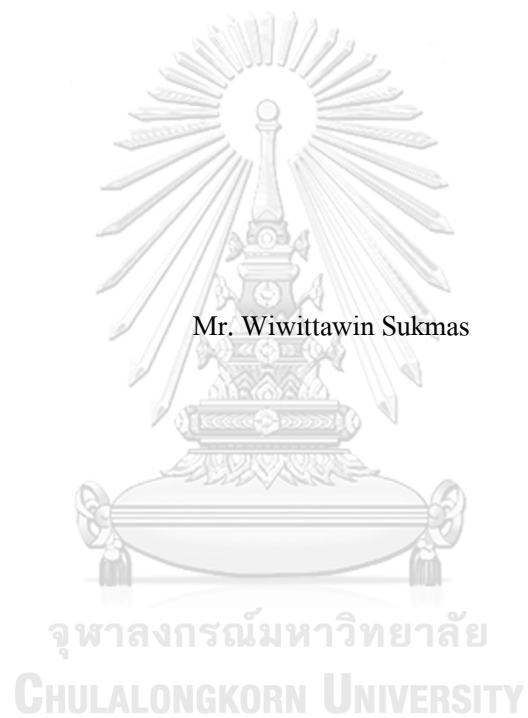


EFFECTS OF ORGANIC MOLECULE ORIENTATIONS ON PEROVSKITE STRUCTURE
OF FORMAMIDINIUM LEAD IODIDE



A Thesis Submitted in Partial Fulfillment of the Requirements

for the Degree of Master of Science in Physics

Department of Physics

Faculty of Science

Chulalongkorn University

Academic Year 2018

Copyright of Chulalongkorn University

ผลของการกำหนดทิศทางของโมเลกุลอินทรีย์ต่อโครงสร้างเพอร์ฟลไกต์ของฟอร์มามิไดเนียมเลด
ไอโอไดด์



วิทยานิพนธ์นี้เป็นส่วนหนึ่งของการศึกษาตามหลักสูตรปริญญาวิทยาศาสตรมหาบัณฑิต
สาขาวิชาฟิสิกส์ ภาควิชาฟิสิกส์
คณะวิทยาศาสตร์ จุฬาลงกรณ์มหาวิทยาลัย
ปีการศึกษา 2561
ลิขสิทธิ์ของจุฬาลงกรณ์มหาวิทยาลัย

Thesis Title	EFFECTS OF ORGANIC MOLECULE ORIENTATIONS ON PEROVSKITE STRUCTURE OF FORMAMIDINIUM LEAD IODIDE
By	Mr. Wiwittawin Sukmas
Field of Study	Physics
Thesis Advisor	Associate Professor Thiti Bovornratanaraks, Ph.D.
Thesis Co Advisor	Associate Professor UDOMSILP PINSOOK, Ph.D.

Accepted by the Faculty of Science, Chulalongkorn University in Partial Fulfillment of
the Requirement for the Master of Science

..... Dean of the Faculty of Science
(Professor POLKIT SANGVANICH, Ph.D.)

THESIS COMMITTEE

..... Chairman
(Assistant Professor SOJIPHONG CHATRAPHORN, Ph.D.)

..... Thesis Advisor
(Associate Professor Thiti Bovornratanaraks, Ph.D.)

..... Thesis Co-Advisor
(Associate Professor UDOMSILP PINSOOK, Ph.D.)

..... Examiner
(Associate Professor NAKORN PHAISANGITTISAKUL,
Ph.D.)

..... Examiner
(Associate Professor Sutee Boonchui, Ph.D.)

วิจิตรวิทย์ สุขมาศ : ผลของการกำหนดทิศทางของโมเลกุลอินทรีย์ต่อโครงสร้างเพอโรฟสไกต์ของฟอร์มามิดิเนียมเลดไอโอไดด์. (EFFECTS OF ORGANIC MOLECULE ORIENTATIONS ON PEROVSKITE STRUCTURE OF FORMAMIDINIUM LEAD IODIDE) อ.ที่ปรึกษาหลัก : รศ. ดร.ชิตี บวรรัตนารักษ์, อ.ที่ปรึกษาร่วม : รศ. ดร.อุดมศิลป์ ปิ่นสุข

Latterly, an emergence of the hybrid organic-inorganic perovskites has captivated an increasing rate of world-wide attention due to their approving physical properties. Formamidinium lead iodide (FAPbI₃), a promising compound owing to its high photovoltaic performance, consists of an organic molecule, i.e. the formamidinium (FA) cation, dwelling in the centre of the cubic unit cell, caged by the inorganic framework, PbI₆. By adopting the *ab initio* method based on the density functional theory including the spin-orbit coupling (SOC) effects, the effects of the FA cation on the cubic FAPbI₃ were thoroughly and systematically investigated. Solidly armed with Euler's rotations, energy landscapes responsible for various sets of orientations of the FA cation were evaluated accordingly. From the energy landscapes, the flipping energy barriers are interpreted as thermal agitations needed to flip the FA cation over. The highest energy barrier amongst all those of other orientations is 24.7 meV which is tantamount to $T \sim 286$ K—the temperature over which the FA molecules randomly reorient. Moreover, it is found that a relatively lowest energy structure when the FA cation is directed along (90°, 60°, 45°) direction. Owing to the structural optimisation, the *I-Pb-I* becomes angled with less than 7°. The *H-I* distances are optimal and confined only in the shells in accordance with the pair distribution function of the optimal configuration. The resulting configuration additionally breaks the inversion symmetry that leads to the Rashba/Dresselhaus effect within the electronic band structure. The largest Rashba splitting parameter determined along the direction in the *k*-space is around 3.0 for the (90°, 60°, 45°) configuration.

สาขาวิชา ฟิสิกส์
ปีการศึกษา 2561

ลายมือชื่อนิสิิต
ลายมือชื่อ อ.ที่ปรึกษาหลัก
ลายมือชื่อ อ.ที่ปรึกษาร่วม

6071996423 : MAJOR PHYSICS

KEYWORD: pair distribution, perovskites, inorganic framework, spin-orbit coupling,
Euler's rotations, Rashba/Dresselhaus effect

Wiwittawin Sukmas : EFFECTS OF ORGANIC MOLECULE ORIENTATIONS
ON PEROVSKITE STRUCTURE OF FORMAMIDINIUM LEAD IODIDE.

Advisor: Assoc. Prof. Thiti Bovornratanaraks, Ph.D. Co-advisor: Assoc. Prof.
UDOMSILP PINSOOK, Ph.D.

เนื่องด้วยสมบัติทางกายภาพที่เป็นที่ยอมรับจากสากล ปรากฏการณ์ที่น่าตื่นตะลึงของเพอโรฟสไกต์ถูกผสมระหว่างสารอินทรีย์และอนินทรีย์ได้ดึงดูดความสนใจอย่างมหาศาล ฟอรัมามิเดียมเลดไอโอไดด์ (FAPI) ซึ่งมีสมรรถภาพทางการเปลี่ยนพลังงานแสงอาทิตย์เป็นไฟฟ้าประกอบไปด้วยสารประกอบอินทรีย์ซึ่งก็คือไอออนบวกฟอรัมามิเดียมดำรงอยู่ที่ศูนย์กลางของยูนิทเซลล์ลูกบาศก์และถูกล้อมไปด้วยโครงอนินทรีย์ PbI_6 ด้วยการใส่ประโยชน์จากทฤษฎีฟังก์ชันนัลของความหนาแน่นกับผลจากการคำนวณของสปินออร์บิต ผลของไอออนบวกฟอรัมามิเดียมที่มีต่อ FAPI ได้ถูกสำรวจตรวจสอบอย่างละเอียดและมีแบบแผนด้วยวิธีการของมูมอัยเลอร์ ภูมิภาคเชิงพลังงานที่ได้จากการวางตัวในทิศทางใดๆของไอออนบวกฟอรัมามิเดียมได้ถูกคำนวณซึ่งมีสันกำแพงเชิงพลังงานที่เกิดขึ้นและสามารถตีความว่าเป็นความร้อนที่ใช้ในการหมุนไอออนบวกฟอรัมามิเดียมโดยที่สันกำแพงที่สูงที่สุดมีค่าเท่ากับ 24.7 มิลลิอิเล็กตรอน โวลต์ซึ่งเทียบเท่ากับอุณหภูมิประมาณ 286 เคลวินและค่านี้คืออุณหภูมิที่ไอออนบวกฟอรัมามิเดียมสามารถที่จะเรียงตัวในทิศทางแบบสุ่ม ยิ่งไปกว่านั้น โครงสร้างของ FAPI ที่มีพลังงานต่ำสุดสัมพัทธ์จะเกิดขึ้นเมื่อไอออนบวกฟอรัมามิเดียมหันไปในทิศทาง ($90^\circ, 60^\circ, 45^\circ$) และจากกระบวนการปรับเชิงโครงสร้างที่เหมาะสมพันธะ *I-Pb-I* มีมุมที่น้อยมากกว่ามุมตรง รูปแบบการเรียงตัวที่ได้ยังก่อให้เกิดการทำลายสมมาตรของโครงสร้าง FAPI ซึ่งส่งผลโดยตรงให้เกิดปรากฏการณ์ที่เรียกว่า “ปรากฏการณ์ราชาบา/เดรสเซลเฮาส์” ในโครงสร้างแถบ โดยที่ค่าการแตกออกแบบราชาบาตามทิศทางใน *k*-space มีค่าประมาณ 3.0 สำหรับรูปแบบการวางตัวของไอออนบวกฟอรัมามิเดียมในทิศทาง ($90^\circ, 60^\circ, 45^\circ$)

Field of Study: Physics

Student's Signature

Academic Year: 2018

Advisor's Signature

Co-advisor's Signature

ACKNOWLEDGEMENTS

I would like to express the deepest appreciation to both of my advisers ever, Assoc. Prof. Dr. Thiti Bovornratanaraks and Assoc. Prof. Dr. Udomsilp Pinsook, who gave me the golden opportunity to do this marvellous project that also helped me in doing a lot of research and I came to know about so many new things I am really grateful of them. Without their guidance and persistent help this thesis would not have been possible.

Secondly, I wish to thank the members of my thesis committee Asst. Prof. Dr. Sojiphong Chatraphorn, Assoc. Prof. Dr. Nakorn Phaisangittisakul, and Assoc. Prof. Dr. Sutee Boonchui for generously offering their time, support, guidance and good will throughout the preparation and review of this document.

Finally, I would also like to thank my parents and colleagues from ECPRL who helped me a lot in finalising this project within the limited time frame.

Wiwittawin Sukmas

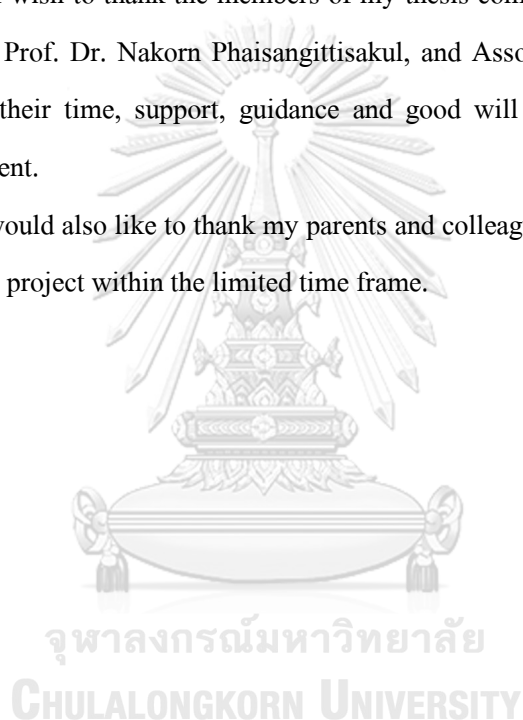


TABLE OF CONTENTS

	Page
ABSTRACT (THAI)	iii
ABSTRACT (ENGLISH).....	iv
ACKNOWLEDGEMENTS.....	v
TABLE OF CONTENTS	vi
LIST OF FIGURES	viii
1. INTRODUCTION	1
2. THEORETICAL BACKGROUND	3
2.1 Many body problems	3
2.2 Density functional theory	5
2.2.1 The Hohenberg-Kohn theorems.....	5
2.2.2 Self-consistent Kohn-Sham equation.....	6
2.2.3 The secular equation.....	9
2.2.4 Techniques of calculation in DFT	10
2.2.4.1 Plane wave basis set.....	10
2.2.4.2 The PAW pseudopotential method.....	11
2.2.4.3 Cutoff energy and k-point mesh	13
2.2.5 Geometry optimisation.....	13
2.2.6 Electronic band structure.....	14
2.2.7 Density of states	15
2.2.8 Spin-orbit interaction.....	15
2.3 Hybrid organic-inorganic perovskites (HOIPs)	16

2.4 Eulerian angles.....	18
3. CALCULATION DETAILS.....	20
3.1 Convergence test of FAPI.....	20
3.2 Relaxed structure of FAPI.....	22
3.3 Euler's rotation applied to relaxed cubic FAPI.....	22
4. RESULTS AND DISCUSSIONS.....	24
4.1 Energy landscapes.....	24
4.2 Pair distribution function for bond-lengths of three structures of FAPI.....	27
4.3 Electronic band structures.....	28
4.4 Projected density of states.....	31
5. CONCLUSION.....	34
APPENDICES.....	35
A. Energy minimisation.....	35
B. Euler's method for the Hartree energy.....	36
C. Atomic coordinates of the input structure of FAPI.....	37
D. Energy landscapes.....	40
E. Equivalent configurations.....	43
REFERENCES.....	2
VITA.....	G

LIST OF FIGURES

	Page
Figure 1: The diagram describing energies theoretically calculated with various methods	5
Figure 2: Schematic diagram for solving self-consistent Kohn-Sham equation	9
Figure 3: The crystal structure of perovskite: ABX_3	16
Figure 4: The crystal structure of HOIP	17
Figure 5: the cubic structure of FAPI (a). The relaxed structure of FAPI (b).....	18
Figure 6: Eulerian angles geometrical definition. The fixed system is shown in black, the rotated system is shown in red. The nodal line (N) is shown in blue	19
Figure 7: The relationship between the total energies and the cutoff energies when k-point is fixed at the value of $4 \times 4 \times 4$	21
Figure 8: The relationship between the total energies and the k-point meshes when cutoff is fixed at the value of 80 Ry	21
Figure 9: The corresponding Eulerian angles for the organic molecule of FA where $C-H$ axis is directed to N-axis (a). First rotation is anti-clockwise through an angle ϕ about the c -axis (b). Second rotation is anti-clockwise through an angle θ about the a' -axis	23
Figure 10: The total energy profile as a function of ϕ , θ , and $\psi = 0^\circ$, taking the lowest total energy as a reference. The scattered data are interpolated adopting Renka-Cline gridding method [47]. The starting point is responsible for $(0^\circ, 0^\circ, 0^\circ)$ configuration.....	25
Figure 11: The total energy profile as a function of ϕ , θ , and $\psi = 45^\circ$, taking the lowest energy as a reference (point A). The scattered data are also interpolated adopting Renka-Cline gridding method [47]. The next higher energy (point B) is responsible for the equivalent lowest energy configuration.	26
Figure 12: The optimum structure of FAPI with the FA cation orienting along $(\phi = 90^\circ, \theta = 60^\circ, \psi = 45^\circ)$ direction.	27

Figure 13: The pair distribution of H–I bonds for three FAPI structures, i.e. unrelaxed, $(0^\circ, 0^\circ, 0^\circ)$, and $(90^\circ, 60^\circ, 45^\circ)$ configurations, respectively.....	28
Figure 14: The electronic band structure of the relaxed FAPI with relaxed $(0^\circ, 0^\circ, 0^\circ)$ –FA molecule. The dashed circle reveals weak interaction between the I atom and the PbI_6 framework.	30
Figure 15: The electronic band structure of the relaxed FAPI with $(90^\circ, 60^\circ, 45^\circ)$ –FA. In the same manner, the dashed circle reveals weak interaction between the I atom and the PbI_6 framework.	30
Figure 16: The projected-density of states for the relaxed FAPI. The relaxed structure with relaxed $(0^\circ, 0^\circ, 0^\circ)$ oriented FA with a peak of I3 shifting leftwards compared to that of the perfect cubic FAPI (a). The corresponding FAPI with $(90^\circ, 60^\circ, 45^\circ)$ –FA (b).	33
Figure 17: α –FAPI	39
Figure 18: relaxed α –FAPI with $(0^\circ, 0^\circ, 0^\circ)$ –FA.....	39
Figure 19: relaxed α –FAPI with $(90^\circ, 60^\circ, 45^\circ)$ –FA.....	39
Figure 20: Energy landscape of $(\phi = 0^\circ, \theta, \psi)$ –FA.....	40
Figure 21: Energy landscape of $(\phi = 15^\circ, \theta, \psi)$ –FA.....	40
Figure 22: Energy landscape of $(\phi = 30^\circ, \theta, \psi)$ –FA.....	41
Figure 23: Energy landscape of $(\phi = 45^\circ, \theta, \psi)$ –FA.....	41
Figure 24: Energy landscape of $(\phi = 60^\circ, \theta, \psi)$ –FA.....	42
Figure 25: Energy landscape of $(\phi = 75^\circ, \theta, \psi)$ –FA.....	42
Figure 26: Energy landscape of $(\phi = 90^\circ, \theta, \psi)$ –FA.....	43
Figure 27: The energy landscape cross section of the $(90^\circ, 60^\circ, 45^\circ)$ –FA configuration.	43

1. INTRODUCTION

Most recently, an emergence of world-wide attention towards hybrid organic-inorganic perovskite (HOIPs) has sharply arisen owing to their potential applications, for instance, in thermoelectric, optoelectronic, and photovoltaic technology, resulting from their astounding electronic, excitonic, and optical properties [1-4]. From 1978 to 2015, there have been some intensive research into the optoelectronic properties of HOIPs and crucial findings in the development of HOIP solar cell [3]. Weber *et al.* were the first to synthesise $MAPbX_3$ ($CH_3NH_3PbI_3$) and determine its crystal structure in 1978 [5]. A couple of decades later, carried out by Mitzi *et al.*, there came syntheses and characterisation of HOIPs for use in electronic devices, specifically optoelectronic devices [6-9]. The first experiment report on a HOIP-based solar cell, $CH_3NH_3PbBr_3$ on a mesoporous TiO_3 surface, was published revealing the solar cell exhibits 3.1% conversion efficiency [10]. The ongoing advancement was followed by tremendous breakthroughs in syntheses and device fabrications of HOIP solar cells [11, 12]. However, the aspect of short-term and long-term stability of this type of material is still a big challenge relating to ambient conditions [13].

It is also suggested that such systems' nature of structure and dynamics, for instance, the presence of supposed ferroelectric domains responsible for reducing rate of electron-hole pair recombination enhances their optoelectronic properties [14] as well as the interaction between the molecular cation and the inorganic framework [15], all impact upon the photovoltaic performance of these very materials. Thus, many researchers have recently attempted to understand these fundamentally structural and motional behaviours that lead to the development of this class of materials towards devices.

Solar cell based on HOIPs, named Formamidinium lead iodide- $HC(NH_2)_2PbI_3$ or FAPI hereafter, has latterly displayed more than 20% of power conversion efficiency which draws attention from many conventional silicon solar cell researchers and delivers marvellous prospects for commercialisation in the near future [16], FAPI, the sister compound of Methylammonium lead iodide or MAPI, exhibits 1.41 eV bandgap energy that is far better matched to solar spectrum than that of MAPI [17].

There has been a myriad of experiments on the synthesis, structure, and phase transitions of FAPI systematically conducted by Stoumpos *et al.* [18]. The material adopts a non-perovskitic structure, hexagonal yellow phase (δ - FAPI), in the space group of $P6_3mc$ at low temperature, whereas its cubic structure is generally formed at higher temperature. Nevertheless, by obtaining data from the single crystal X-ray diffraction, Weller *et al.* have strongly confirmed that FAPI crystallises at room temperature as a cubic phase (α -phase) [19]. Moreover, atomic positions of FAPI investigated by using Neutron powder diffraction reveals that the trigonal planar $HC(NH_2)_2^+$ or the FA cation lies in the central mirror plane of the unit cell where it orientates over 12 equivalent sites so that the $C - H$ bond is directed into a cubic face [19]. In addition, FAPI was observed to have a thermal hysteresis for the cubic-to-hexagonal phase transition and was also demonstrated that FAPI can be kinetically trapped and remains in a meta-stable state, namely cubic state, upon temperature quenching from 400 K down to 8.2 K [20]. It was additionally reported that the FA cation randomly reorients over 480 sites [20] instead of 12 sites as previously suggested by Weller *et al.* [19].

As extensively mentioned above, not only has there been a plethora of evidences supporting the existence of the molecular dynamics of the FA cation in FAPI, but also does the investigation into effects of diverse orientations of the organic molecule on the well-known HOIPs, MAPI, which reported that MAPI exhibits indirect bandgaps owing to the effect of strain induced by interaction between the organic molecular orientations and the inorganic framework, i.e. PbI_6 [21]. Apart from experimental results, many calculations regarding the rotational effects of $CH_3NH_3^+$ on MAPI have been made [22, 23] and revealed Rashba Splitting causing an indirect bandgap in HOIPs [24]. Because of these phenomena, the effect of the organic molecule's arrangements must play a crucial role in structural stability and other physical properties of these hybrid materials.

The objectives of this thesis is to use the *Ab initio* calculations based on the state-of-the-art density functional theory (DFT) [25] to investigate effects of the FA cation on cubic FAPI, together with applying rigid flips through Euler's rotation on the organic molecule. The energy landscape schemes accounting for the FA cation's different orientations will be elucidated as well as the electronic band structures.

2. THEORETICAL BACKGROUND

In this chapter, extensively, all theoretical background employed in this thesis are discussed. In Section 2.2, the major technique used in this work, the so-called ‘‘Density Functional Theory’’, will be covered in detail.

2.1 Many body problems

With the help of quantum mechanics, one is able to describe the microscopic properties of condensed matters by solving the well-known time-dependent Schrödinger equation. Yet for many body problems, since systems in reality always contain a large number of atoms ($\sim 10^{23}$ atoms), to solve for the exact solution of such systems are cumbersome and almost impossible at the moment. The time-independent Schrödinger equation in Hartree atomic units is given by;

$$\hat{\mathcal{H}}\Psi(\mathbf{r}_1, \mathbf{r}_2, \dots, \mathbf{r}_{N_e}, \mathbf{R}_1, \mathbf{R}_2, \dots, \mathbf{R}_{N_n}) = E\Psi(\mathbf{r}_1, \mathbf{r}_2, \dots, \mathbf{r}_{N_e}, \mathbf{R}_1, \mathbf{R}_2, \dots, \mathbf{R}_{N_n}), \quad (2.1)$$

where \hat{H} is the Hamiltonian of the many-body system,

$$\hat{\mathcal{H}} = -\frac{1}{2} \sum_{i=1}^n \nabla_i^2 - \frac{1}{2} \sum_{I=1}^N \frac{1}{M_I} \nabla_I^2 - \sum_{i,I} \frac{Z_I}{|\mathbf{r}_i - \mathbf{R}_I|} + \frac{1}{2} \sum_{i \neq j} \frac{1}{|\mathbf{r}_i - \mathbf{r}_j|} + \frac{1}{2} \sum_{I \neq J} \frac{Z_I Z_J}{|\mathbf{R}_I - \mathbf{R}_J|} \quad (2.2)$$

The small and capital letters denote electron and nuclei, respectively. The first two terms on right-hand side of Eq. (2.2) are the kinetic energy of electrons and of the nuclei, respectively, where M_I represents the mass of the nucleus at site I . The following three terms are responsible for Coulomb interactions of electron-nucleus, electron-electron, and nucleus-nucleus, respectively, since both electrons and nuclei are electrically charged particles. The vector \mathbf{r}_i denotes the position of electron at site i , whereas \mathbf{R}_I and Z_I refer to the position and the charge number of the nucleus at site I , respectively.

According to the *Born-Oppenheimer* approximation [26], the effect from nuclei in electronic problem can be omitted at this point, since the nuclei are much heavier than the electrons, so they move more slowly. In other words, to the electrons the ions are essentially stationary. Therefore, the kinetic term accounting for the nuclei is separated, and the nucleus-

nucleus interaction term becomes a constant which will as well be taken into consideration separately. The problem now to be solved is the Schrödinger equation for electrons, which can be written as

$$\hat{\mathcal{H}}_e \Psi_e(\mathbf{r}, \mathbf{R}) = E_e \Psi_e(\mathbf{r}, \mathbf{R}), \quad (2.3)$$

where

$$\hat{\mathcal{H}} = -\frac{1}{2} \sum_{i=1}^n \nabla_i^2 - \sum_{i,I} \frac{Z_I}{|\mathbf{r}_i - \mathbf{R}_I|} + \frac{1}{2} \sum_{i \neq j} \frac{1}{|\mathbf{r}_i - \mathbf{r}_j|}, \quad (2.4)$$

where $\Psi_e(\mathbf{r}, \mathbf{R})$ and E_e are the electron wave function and eigenvalues, respectively.

So far the number of variables in the N_e -body wave function has been reduced to $3N_e$, yet it is still problematic for solving Eq. (2.3). That being said, the many-electron wave function can be purely obtained from a product of single-electron wave function as proposed by Hartree in 1928 [27]. However, this theory fails to describe the true nature of electronic properties due to the violation of the anti-symmetry of the wave function—electrons are fermions—which in turn implicitly lifts the ground state energy. An improvement from Hartree theory is known as the Hartree Fock (HF) theory [28]. In the HF theory, the HF wave function was proposed as a determinant of many single-electron wave functions named “Slater determinant”, explicitly including the anti-symmetry of the wave function.

$$\Psi_{HF} = \frac{1}{N!} \det \begin{pmatrix} \psi_1(\mathbf{r}_1) & \psi_2(\mathbf{r}_1) & \cdots & \psi_N(\mathbf{r}_1) \\ \psi_1(\mathbf{r}_2) & \psi_2(\mathbf{r}_2) & \cdots & \psi_N(\mathbf{r}_2) \\ \vdots & \vdots & \ddots & \vdots \\ \psi_1(\mathbf{r}_N) & \psi_2(\mathbf{r}_N) & \cdots & \psi_N(\mathbf{r}_N) \end{pmatrix} \quad (2.5)$$

Although the total energy calculated employing HF theory is theoretically lower than that obtained from Hartree method, the energy is still higher than the exact one. It is also worth noting that the difference of energies calculated with the Hartree and HF methods is the “exchange energy”, whereas it is called the “correlation energy” when being the difference between the energy calculated with HF method and the true ground state, see Figure 1.

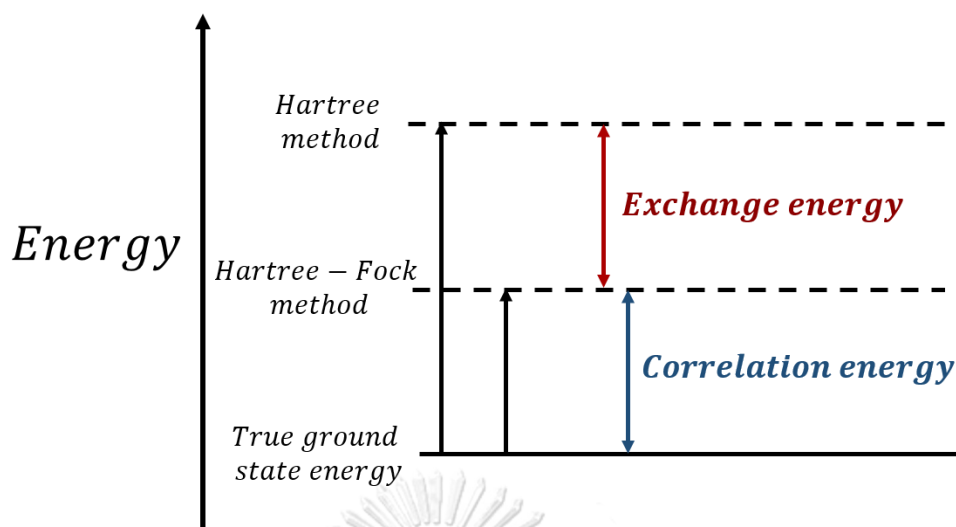


Figure 1: The diagram describing energies theoretically calculated with various methods

By the way, the HF theory has various drawbacks, for instance, it is not suitable for systems containing a large number of electrons owing to the consumption of huge memory resources and expensive computational costs. Fortunately, enough, the density functional theory (DFT) is introduced as a hopeful and appropriate tool with which one is allowed to solve the many-electron problems. In the followings, a description of this reliable method will be discussed.

2.2 Density functional theory

The Density functional theory (DFT), first proposed in the year of 1964 by P. Hohenberg and W. Kohn [25], is one of most popular and successful approach in investigating ground-state energies and electronic structures accounting for many-body quantum systems. Despite being the exact method, it needs, in principle, some approximations for exchange-correlation functionals. In the followings, a description of the DFT will be discussed in detail.

2.2.1 The Hohenberg-Kohn theorems

Hohenberg and Kohn formulated two theorems that has been known to be the starting point of the DFT. The two theorems are stated [25] as follows:

Theorem I: For any system of interacting particles in an external potential $V_{ext}(\mathbf{r})$, there is a one-to-one correspondence between the external potential and ground-state density, $n(\mathbf{r})$. In addition, the ground-state expectation value of any observable quantity A is a unique function.

$$\langle \Psi | \hat{A} | \Psi \rangle = A[n_0(\mathbf{r})] , \quad (2.6)$$

The theorem implies that the density parameter is the only variable being taken into account for DFT instead of the wave function for Hartree-Fock theory.

Theorem II: For an arbitrarily external potential applied to an interacting system, it is feasible to exactly define a universal total energy functional of the particle density, which is given as,

$$\mathcal{E}[n(\mathbf{r})] = E_{HK}[n(\mathbf{r})] + \int V_{ext}(\mathbf{r}) n(\mathbf{r}) d\mathbf{r}, \quad (2.7)$$

where E_{HK} is the universal constant that does not completely relate to any information of any types of nuclei or their positions. This hereby means it is considered as an arbitrarily universal constant for the interacting system, yet it is unknown. Assuming the constant is given, the ground-state energy can be determined by minimising total energy with respect to density with an employment of the variational principle,

$$\left. \frac{\delta \mathcal{E}[n(\mathbf{r})]}{\delta n} \right|_{n=n_0} = 0. \quad (2.8)$$

The exact ground-state energy, \mathcal{E}_0 , corresponding to the ground-state density $n_0(\mathbf{r})$ is given by

$$\mathcal{E}_0 = \mathcal{E}[n_0(\mathbf{r})] \leq \mathcal{E}[n(\mathbf{r})]. \quad (2.9)$$

2.2.2 Self-consistent Kohn-Sham equation

According to the Hohenberg-Kohn theorem, the density parameter is used as the main quantity for calculating all observables. In the year of 1965, Kohn and Sham proposed a brand new Schrödinger-like equation, namely “Kohn-Sham equation”, as a function of density [29]. One can employ the electron density $n(\mathbf{r})$ as a basic variable in lieu of solving for many-electron wave function Ψ_e in Eq. (2.3). The energy functional is given as,

$$\mathcal{E}[n(\mathbf{r})] = T_0[n(\mathbf{r})] + \frac{1}{2} \iint \frac{n(\mathbf{r})n(\mathbf{r}')}{|\mathbf{r} - \mathbf{r}'|} d\mathbf{r}d\mathbf{r}' + \int V_{ext}(\mathbf{r})n(\mathbf{r})d\mathbf{r} + E_{xc}[n(\mathbf{r})]. \quad (2.10)$$

The first term on the right-hand side is non-interacting kinetic energy functional, responsible for all electrons in the system. The second term arises from the electron-electron interaction, known as Hartree energy. As for the third term, the external potential energy is due to nuclei and the inner shells' electrons. Finally, the last term is nothing but the exchange-correlation energy.

Within the Kohn-Sham scheme, the particle density $n(\mathbf{r})$ of the system with non-interacting particles can be obtained as

$$n(\mathbf{r}) = \sum_{i=1}^N |\Psi_i^{KS}(\mathbf{r})|^2 = \sum_{i=1}^N \Psi_i^{*KS}(\mathbf{r}) \Psi_i^{KS}(\mathbf{r}). \quad (2.11)$$

The total energy in Eq. (2.10) is blatantly the functional of $n(\mathbf{r})$ and/or $\Psi_i(\mathbf{r})$. Thus the ground-state energy can be obtained by minimising $\mathcal{E}[n(\mathbf{r})]$ with respect to the density in accordance with Eq. (2.9). The energy minimisation can be achieved by adopting the Euler's equation with a Lagrange multiplier (λ_i), see Appendices for a rigorous derivation. For now, the Kohn-Sham orbital (in atomic unit) is written as

$$\left[-\frac{\nabla_i^2}{2} + V_{eff}(\mathbf{r}) \right] \Psi_i^{KS}(\mathbf{r}) = \mathcal{E} \Psi_i^{KS}(\mathbf{r}), \quad (2.12)$$

where the effective potential is given by

$$V_{eff}(\mathbf{r}) = V_{ext}(\mathbf{r}) + V_H[n(\mathbf{r})] + V_{xc}[n(\mathbf{r})], \quad (2.13)$$

with

$$V_H[n(\mathbf{r})] = \int \frac{n(\mathbf{r}')}{|\mathbf{r} - \mathbf{r}'|} d\mathbf{r}'$$

and

$$V_{xc}[n(\mathbf{r})] = \frac{\delta E_{xc}[n(\mathbf{r})]}{\delta n}.$$

The Kohn-Sham equation allows one to investigate complex quantum systems by completely mapping an interacting system into a fictitious no-interacting system in which the particle is dwelling. Note that, the Kohn-Sham orbital, $\Psi_i^{KS}(\mathbf{r})$, is not the wave function of the system, the density obtained from the Kohn-Sham orbitals, however, is the exact density of the true system.

To solve the Kohn-Sham equation, described by flowchart in Figure 2, firstly, the initial value of the density is guessed in order to obtain the effective potential. Secondly, the equation is solved to output the total energies and the Kohn-Sham orbitals. Afterwards, the new density is subsequently obtained from the just-calculated Kohn-Sham orbitals and then used for next step. This iterative process runs self-consistently until the convergence criterion of density is fulfilled. Finally, the output quantities, e.g. band structures and density of states, are calculated via the converged density.

In Eq. (2.13), the first two terms, $V_{ext}(\mathbf{r})$ and $V_H(\mathbf{r})$, are able to be exactly evaluated, whereas the last term, $V_{xc}[n(\mathbf{r})]$, is still unknown, which must be modelled. The exchange-correlation potential, $V_{xc}[n(\mathbf{r})]$, contains all unknown information—all the quantum mechanical and explicit many-body effects.

As for the conventional exchange-correlation functions, there are two types of well-known methods, namely the Local Density Approximation (LDA) and the Generalised Gradient Approximation (GGA).

➤ **Local Density Approximation (LDA):** By far the simplest way to derive $E_{xc}[n]$ is the scheme called the local density approximation, wherein the exchange-correlation functional is directly derived from the homogeneous electron gas [30]. The method works quite efficiently for slow varying density, e.g. free electron-gas-like systems. Practically, LDA approximates $E_{xc}[n]$ by assuming the exchange-correlation energy density, $\epsilon_{xc}^{LDA}[n(\mathbf{r})]$, at any point \mathbf{r} in space is of the same form as the homogeneous electron gas, $\epsilon_{xc}^{hom}[n(\mathbf{r})]$, which has been profoundly studied adopting Green's-function Monte Carlo method [31]. The proposed approximation is thus given by

$$E_{xc}^{LDA}[n(\mathbf{r})] = \int n(\mathbf{r}) \epsilon_{xc}^{hom}[n(\mathbf{r})] d\mathbf{r}. \quad (2.14)$$

Nevertheless, it is conventionally not appropriate in using LDA in many cases, for instance, in the case of rapidly-varying density systems—more complex systems.

➤ **Generalised Gradient Approximation (GGA)**

In real systems, mostly, the electron density is unlikely to be homogeneous and it is therefore impractical for LDA scheme to be applied in many cases. There are, nevertheless, many attempts to improve the LDA by considering higher-order terms of the exchange-correlation energy. Consequently, not only is the electron density, $n(\mathbf{r})$, included in the exchange-correlation energy, but the gradient of density, $\nabla n(\mathbf{r})$, is also taken into account, which is expressed as

$$E_{xc}^{GDA}[n(\mathbf{r})] = \int n(\mathbf{r}) \epsilon_{xc}[n(\mathbf{r}), \nabla n(\mathbf{r})] d\mathbf{r}. \quad (2.15)$$

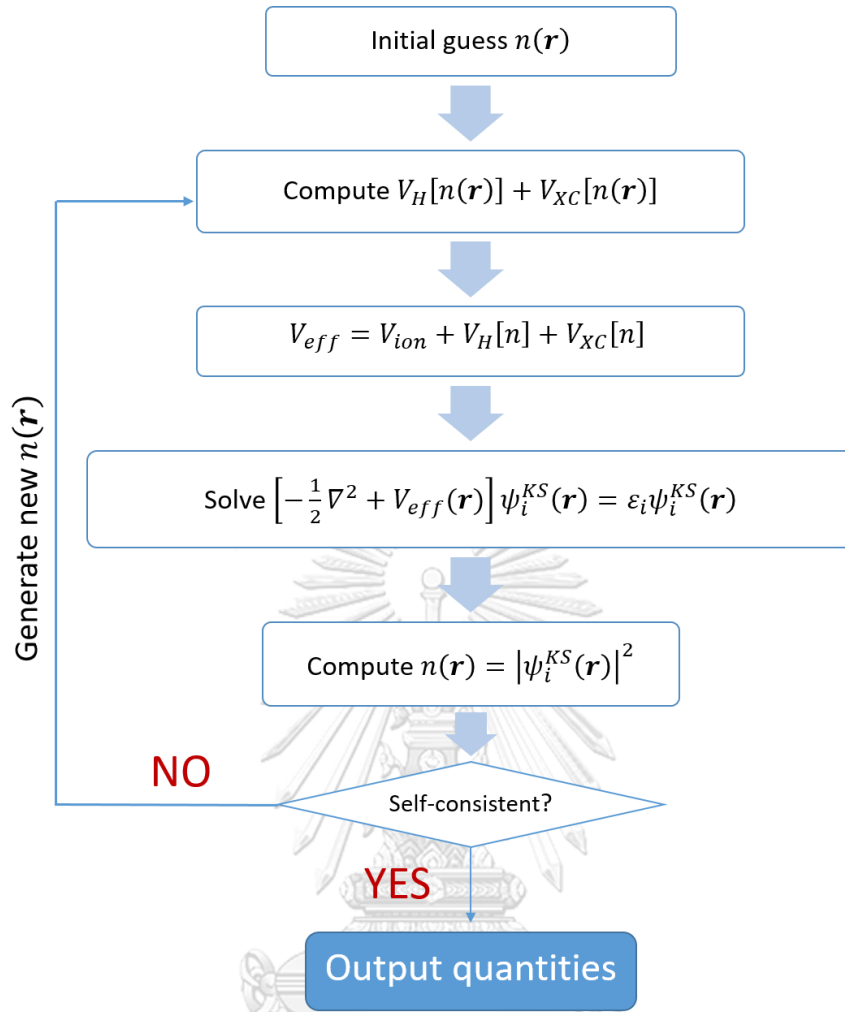


Figure 2: Schematic diagram for solving self-consistent Kohn-Sham equation

2.2.3 The secular equation

In order to solve for the Kohn-Sham equation, the method for obtaining the solutions is described as follows: Firstly, the Kohn-Sham orbitals are expressed as a linear combination of arbitrary basis function,

$$\Psi_n(\mathbf{r}) = \sum_{i=1}^Q C_i^n \varphi_i(\mathbf{r}), \quad (2.16)$$

where C_i^n are sets of coefficients and $Q \rightarrow \infty$; practically, however, Q is always set to be as possibly large as to increase a degree of accuracy of the Kohn-Sham orbitals. Subsequently, the Kohn-Sham orbitals are substituted into the Kohn-Sham equation, Eq. (2.12), as follows:

$$\sum_{i=1}^Q C_i^n \left[-\frac{\nabla_i^2}{2} + V_{eff}(\mathbf{r}) \right] \varphi_i(\mathbf{r}) = \sum_{i=1}^Q C_i^n \varepsilon_i \varphi_i(\mathbf{r}) \quad (2.17)$$

Next, Eq. (2.17) is multiplied by the complex conjugate of the basis function, $\varphi_j^*(\mathbf{r})$, and integrated over all space, written as

$$\sum_{i=1}^Q C_i^n \int \varphi_j^*(\mathbf{r}) \left[-\frac{\nabla_i^2}{2} + V_{eff}(\mathbf{r}) \right] \varphi_i(\mathbf{r}) d\mathbf{r} = \sum_{i=1}^Q C_i^n \varepsilon_i \int \varphi_j^*(\mathbf{r}) \varphi_i(\mathbf{r}) d\mathbf{r}. \quad (2.18)$$

Eq. (2.18) can be viewed as a matrix form, where the integral on the left-hand side is represented as the Hamiltonian matrix, \mathcal{H} , and the overlap matrix, \mathcal{O} , being on the right-hand side. Now it can thus be written as

$$\mathcal{H}\mathcal{C} = \varepsilon\mathcal{O}\mathcal{C}, \quad (2.19)$$

which is known as the “secular equation”. The Hamiltonian matrix and the overlap matrix are the $Q \times Q$ dimensional matrices. This eigenequation can be solved using several methods. And, lastly, the Q eigenvalues and the Q sets of eigenfunctions are obtained and they are used as primary inputs for determining further interested quantities.

2.2.4 Techniques of calculation in DFT

2.2.4.1 Plane wave basis set

In solid, there are a variety of defects causing difficulties in solving the Kohn-Sham equation of real solid. If one considers only a periodic solid, invariant under translational and rotational symmetries, this complex problem can be simplified by exploiting Bloch theorem [32]. In Bloch theorem, the electron wave function being the solutions of the Schrödinger equation is plane waves multiplied with a periodic function $u_k^n(\mathbf{r})$ as

$$\Psi_k^n(\mathbf{r}) = u_k^n(\mathbf{r}) e^{i\mathbf{k}\cdot\mathbf{r}}, \quad (2.20)$$

where \mathbf{k} is a wave vector and n is a band index. The wave function and energy eigenvalue must fulfil these conditions:

$$\mathcal{E}(\mathbf{k}) = \mathcal{E}(\mathbf{k} + \mathbf{G}), \quad (2.21)$$

$$\Psi_k^n(\mathbf{r}) = \Psi_{\mathbf{k}+\mathbf{G}}^n(\mathbf{r}), \quad (2.22)$$

with \mathbf{G} being the reciprocal lattice vector. Consequently, the maximum value of \mathbf{G} , \mathbf{G}_{max} , is related to the kinetic cutoff energy by the expression:

$$\mathcal{E}_{max} = \frac{\hbar^2 \mathbf{G}_{max}^2}{2m}. \quad (2.23)$$

As for the periodic function, it is defined as a summation over plane wave sets,

$$u_k^n(\mathbf{r}) = \sum_j C_j^n(\mathbf{k}) e^{i\mathbf{G}_j \cdot \mathbf{r}}. \quad (2.24)$$

By plugging Eq. (2.24) into Eq. (2.20), the volumetric normalised electron wave function is conclusively written as

$$\Psi_k^n(\mathbf{r}) = \frac{1}{\sqrt{V}} \sum_j C_j^n(\mathbf{k}) e^{i(\mathbf{k} + \mathbf{G}_j) \cdot \mathbf{r}}. \quad (2.25)$$

2.2.4.2 The PAW pseudopotential method

The Projected Augmented Wave or PAW method was adopted throughout the work. This method was methodically adopted from the augmented plane wave method by separating the wave function into two parts: partial wave expansions inside the sphere and envelope function outside the sphere [33]. The envelope function must be differentiable and totally matched at the sphere boundary. Since having countless number of partial waves close to the atomic core, the all-electron wave function, Ψ , is in turn mapped into a fictitious smooth function which is known as auxiliary wave function, $\tilde{\Psi}$, consisting of a smaller number of the partial wave basis. Within the sphere of volume Ω_R , each of the wave function and the fictitious smooth wave function can be expanded as a linear combination of the partial wave basis set:

$$|\Psi(\mathbf{r})\rangle = \sum_i a_i |\phi_i(\mathbf{r})\rangle, \text{ inside } \Omega_R \quad (2.26)$$

and

$$|\tilde{\Psi}(\mathbf{r})\rangle = \sum_i b_i |\tilde{\phi}_i(\mathbf{r})\rangle, \text{ inside } \Omega_R. \quad (2.27)$$

whereas the all-electron partial wave and the auxiliary partial wave outside the sphere are identical:

$$\phi_i(\mathbf{r}) = \tilde{\phi}_i(\mathbf{r}). \text{ outside } \Omega_R \quad (2.28)$$

The all-electron partial wave is the solution solved from the radial Schrödinger equation for an isolated atom and the auxiliary wave function can be chosen from the all-electron partial wave that match the all-electron partial wave outside the sphere. Accordingly, the all-electron wave function and the auxiliary wave function are connected via the transformation operator, τ .

$$|\Psi\rangle = \tau|\tilde{\Psi}\rangle, \quad (2.29)$$

the transformation operator can be defined as

$$\tau = \hat{\mathbf{1}} + \sum_R S_R. \quad (2.30)$$

As defined in Eq. (2.30), the transformation operator can generally be obtained by combining the identity operator ($\hat{\mathbf{1}}$) with a sum of the atomic contribution (S_R) at each particular site R . The atomic contribution reflects the difference between all-electron partial wave and the auxiliary partial wave, that is to say,

$$S_R|\tilde{\phi}_i\rangle = |\phi_i\rangle - |\tilde{\phi}_i\rangle. \quad (2.31)$$

Now the new operator needed to be defined: $|\tilde{P}_i\rangle$ as the projector operator expressing the local character of a wave function in the atomic region [34]. The operator is bound to be orthonormal to the smooth partial wave basis set,

$$\langle \tilde{P}_m | \tilde{\phi}_n \rangle = \delta_{mn}.$$

By using the mentioned property, the smooth wave function can be written as

$$|\tilde{\Psi}\rangle = \sum_i |\tilde{\phi}_i\rangle \langle \tilde{P}_i | \tilde{\Psi}\rangle. \quad (2.32)$$

By applying Eq. (2.30) into (2.32), we have

$$|\Psi\rangle = \left(\hat{\mathbf{1}} + \sum_i (|\phi_i\rangle - |\tilde{\phi}_i\rangle) \langle \tilde{P}_i | \right) |\tilde{\Psi}\rangle. \quad (2.33)$$

As a result, the transformation operator in also written as

$$\tau = \hat{\mathbf{1}} + \sum_i (|\phi_i\rangle - |\tilde{\phi}_i\rangle) \langle \tilde{P}_i |. \quad (2.34)$$

Now consider an arbitrary operator represented as A , the expectation value of A :

$$\begin{aligned}
\langle A \rangle &= \sum_n f_n \langle \Psi_n | A | \Psi_n \rangle, \\
&= \sum_n f_n \langle \Psi_n | \tau^\dagger A \tau | \Psi_n \rangle.
\end{aligned} \tag{2.35}$$

The occupation number is denoted by f_n . To apply the PAW approach to the Kohn-Sham equation, this very equation can be rearranged as

$$(\tilde{\mathcal{H}} - \varepsilon \tilde{\mathcal{S}}) |\tilde{\Psi}\rangle = 0, \tag{2.36}$$

where $\tilde{\mathcal{H}} = \tau^\dagger \mathcal{H} \tau$ and $\tilde{\mathcal{S}} = \tau^\dagger \tau$ operators are represented as pseudo-Hamiltonian and overlap matrix, respectively

2.2.4.3 Cutoff energy and k -point mesh

The reciprocal space, known as \mathbf{k} -space, represents the Fourier transform of the repetitive periodic lattice in the real space. In this work, the Kohn-Sham equation is solved within reciprocal space using plane waves for basis sets. The infinite number of the plane-wave basis sets in Eq. (2.25) gives the exact solution of the Kohn-Sham equation. It is, nevertheless, impossible to evaluate the exact solution due to limited computational resources. Therefore, the limited yet suitable number of plane-wave basis sets, as proposed by Monkhorst and Pack [35], is conditioned by the kinetic cutoff energy, E_{cut} , which is defined through the maximum value of the reciprocal lattice vector, \mathbf{G}_{max} . Now the kinetic energy cutoff is written as

$$E_{cut} \leq \frac{\hbar^2}{2m} |\mathbf{k} + \mathbf{G}_{max}|^2. \tag{2.37}$$

The larger the number of the kinetic cutoff energies and the k -points, the more accurately the energy is evaluated; it also requires more computational resources.

2.2.5 Geometry optimisation

The geometry optimisation is the process of finding an arrangement in space of crystal structures where they are of minimum energies [36]. The considered structure is relaxed so that the net interatomic force on each atom is satisfactorily close to zero the atomic positions are stationary points. However, in DFT, the temperature is not taken into account, the system in contact with any value of pressure and $T = 0 \text{ K}$ reservoirs prefers the minimum enthalpy, as given,

$$\mathcal{H} = E + P\Omega. \quad (2.38)$$

The strain components are of 9 dimensions, together with $3N$, thus the enthalpy is now of the functional of $(9 + 3N)$ -dimensional space:

$$\mathcal{H} = \mathcal{H}(\epsilon, \mathbf{r}_1, \mathbf{r}_2, \mathbf{r}_3, \dots, \mathbf{r}_N). \quad (2.39)$$

The first derivative of the enthalpy with respect to the coordinates of atoms, X_i , gives rise to the force vector, which is written as

$$F = - \left. \frac{\partial \mathcal{H}}{\partial X} \right|_P. \quad (2.40)$$

The variation of enthalpy around the minimum X_{min} is defined as

$$\delta \mathcal{H} = \frac{1}{2} (X - X_{min}) \cdot B (X - X_{min}), \quad (2.41)$$

where B denotes the Hessian matrix. The quasi-Newton method [36] being used to simultaneously relax lattice parameters and the internal coordinates of crystals under pressure helps search for the X_{min} from the force in one relaxation step. The X_k is improve to obtain X_{min} through the equation

$$\Delta X_k = H_k F_k, \quad (2.42)$$

where $H = B^{-1}$. Despite H_0 being unknown, it can be speculated and updated by the BFGS method [37]. When X reaches its minimum, the crystal structure then satisfies the external pressure and it also has the minimum enthalpy which is evaluated through the aforementioned algorithm.

2.2.6 Electronic band structure

The solution of the Kohn-Sham equation, Eq. (2.12), outputs the ground-state wave function, $\Psi_k^n(\mathbf{r})$, and is also corresponding to the Hamiltonian of the system. Then, the electronic properties of the system are obtained by evaluating the expectation values of the total energy responsible for any \mathbf{k} -vector, which is given by

$$\langle \Psi_{nk'} | \hat{\mathcal{H}} | \Psi_{nk} \rangle = \epsilon_{nk} \delta_{kk'}. \quad (2.43)$$

After obtaining energies corresponding to each value of \mathbf{k} , the electronic band structure is determined by plotting this set of energy eigenvalues along the high symmetry points in the first Brillouin zone.

2.2.7 Density of states

The density of states (DOS) describes the number of states which are available to be occupied by the system at each level of energy. It is mathematically interpreted as a distribution via a probability density function. The DOS for a given n^{th} -energy level, $g(\varepsilon)$, is expressed as

$$g_n(\varepsilon) = \int \frac{d\mathbf{k}}{4\pi^3} \delta(\varepsilon - \varepsilon_n(\mathbf{k})), \quad (2.44)$$

where the integral is all over any primitive cell, $\varepsilon_n(\mathbf{k})$ denotes the energy eigenvalue accounting for the n^{th} -energy level. In the same manner, the partial density of states (pDOS) corresponds to the projection of any particular orbital of the particular atom on the density of states.

2.2.8 Spin-orbit interaction

In hydrogen-like atoms, the central potential, as neglecting spin, suitable for the valence electron is no longer of the pure Coulomb form. Since the electrostatic potential, $\phi(r)$, presenting in

$$V_c(\mathbf{r}) = e\phi(\mathbf{r}) \quad (2.45)$$

is no longer due only to the nucleus of the electric charge $|e|Z$; the cloud of negatively charged electrons in the inner shells must be taken into account. Electrostatically, this results from the fact that the higher angular momentum states are more susceptible to the repulsion due to the electron cloud. Now the valence electron experiences the electric field

$$\mathbf{E} = -\left(\frac{1}{e}\right) \nabla V_c(\mathbf{r}). \quad (2.46)$$

Nevertheless, electrodynamically, a moving charge subjected to an electric field feels an effective magnetic field given by

$$\mathbf{B}_{eff} = -\left(\frac{v}{c}\right) \times \mathbf{E}. \quad (2.47)$$

And since the electron has a magnetic dipole moment, $\boldsymbol{\mu} = e\mathbf{S}/m_e c$. By plugging Eqs. (2.45) and (2.46) into the Hamiltonian of the dipole, this gives rise to the following interaction energy:

$$H_{SOC} = -\boldsymbol{\mu} \cdot \mathbf{B}_{eff} = \frac{1}{2m_e^2 c^2} \frac{1}{r} \frac{dV_c}{dr} (\mathbf{L} \cdot \mathbf{S}).. \quad (2.48)$$

A factor of 2 is corrected in order that the energy includes the precession of the electron's spin moment, which is relativistic effect when in the absence of an external magnetic field. The rigorous derivation, however, is traced back to the original work proposed by L. H. Thomas [38]. The SOC Hamiltonian, H_{SOC} , will be added in the Kohn-Sham equation, Eq. (2.12), as a correction term in order to precisely evaluate the system's total energies and the electronic band structures.

2.3 Hybrid organic-inorganic perovskites (HOIPs)

Materials with the formula ABX_3 , wherein situates cations A and B including an anion X , are called perovskites. The ideal crystal structure of perovskite, as illustrated in Figure 3, consists of a corner-sharing tetrahedral cage, BX_6 , with a linear $B - X - B$ bond and A ions in the interstitial positions [39].

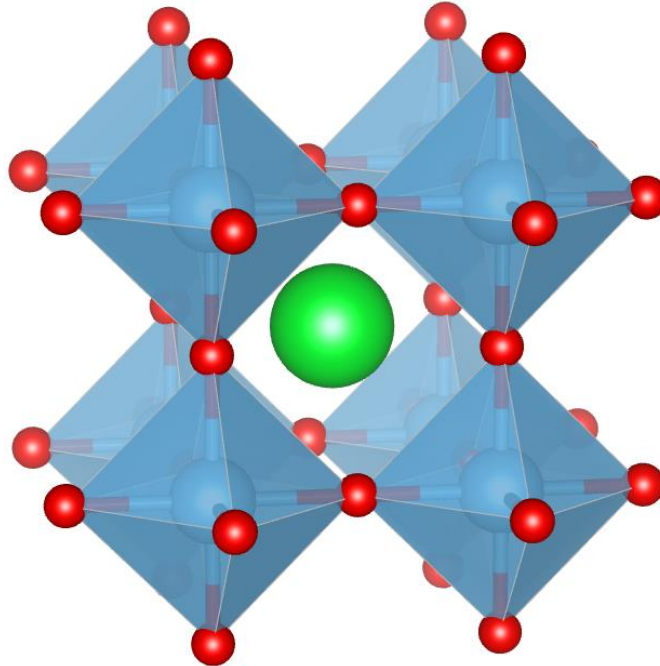


Figure 3: The crystal structure of perovskite: ABX_3

As for the hybrid organic-inorganic perovskites, A happens to be a monovalent organic cation [3]. The synthesis and the determination of crystal structure of $CH_3NH_3PbI_3$ was first reported by Weber [5], the usage of HOIPs in optoelectronic devices subsequently happened [7], while the

power conversion efficiencies accounting for the HOIP solar cell were 4% and 20% for the year of 2009 and 2015, respectively [7-9]. These fascinating performances of HOIPs have thus stimulated bunches of HOIP-related research to be proliferating until now.

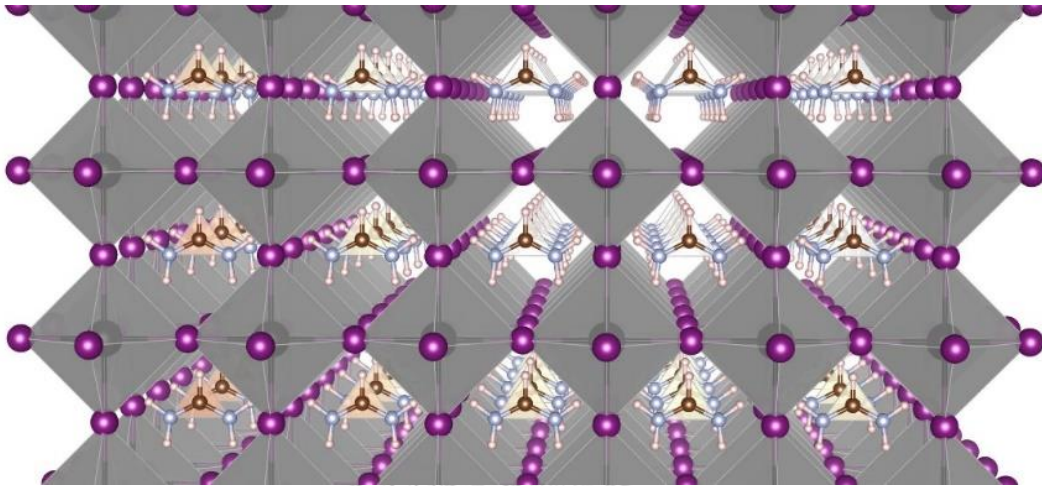


Figure 4: The crystal structure of HOIP

In this work, Formamidinium lead iodide, $HC(NH_2)_2PbI_3$ or FAPI, was systematically and thoroughly investigated. FAPI adopts a non-perovskitic structure, hexagonal yellow phase (α -FAPI), in the space group $P6_3mc$ at low temperature, whereas its cubic structure depicted in Figure 4 is formed at higher temperature [18], it however was demonstrated that FAPI can be kinetically trapped and remained in a meta-stable state, namely cubic state, upon temperature quenching from 400 K to 8.2 K [20]. Thus, we are solely focusing on the investigation of the physical properties of α -FAPI. The $Pm\bar{3}m$ structure of α -FAPI, shown in Figure 5(a), with an experimentally reported lattice constant of 3.3613 Å [19]. The organic molecule, the Formamidinium (FA) cation, lies in the central mirror plane of the unit cell, wherein it randomly reorients over 480 possible sites as suggested by Chen *et al.* [20].

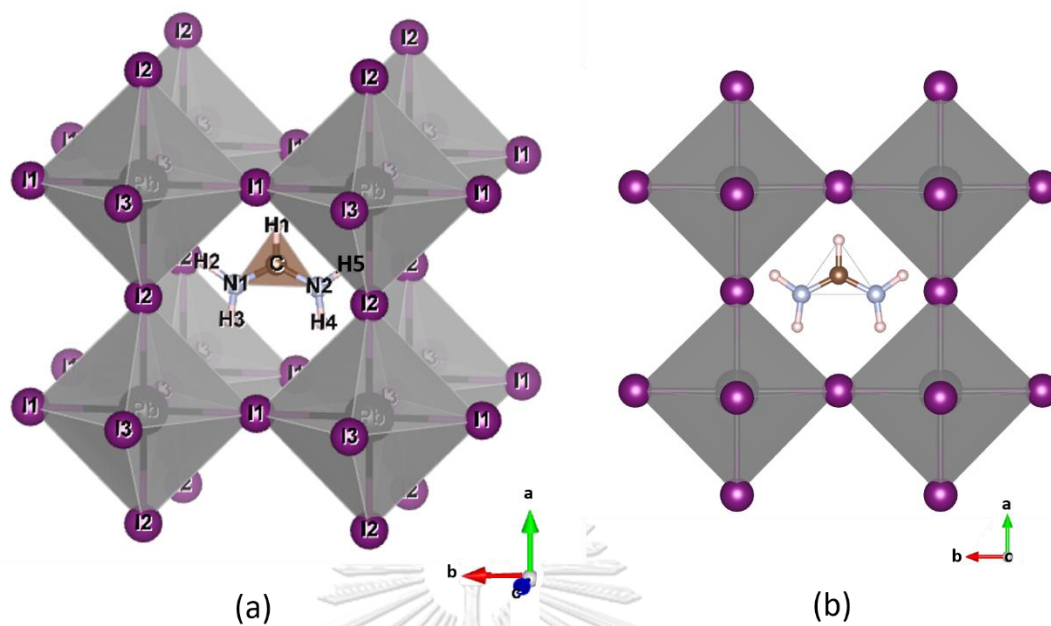


Figure 5: the cubic structure of FAPI (a). The relaxed structure of FAPI (b).

2.4 Eulerian angles

To transform one coordinate system to another can be represented by a matrix equation of the form

$$\mathbf{r}' = \boldsymbol{\lambda} \mathbf{r}$$

The fixed system is identified with \mathbf{r} and the rotated system with \mathbf{r}' , then the rotation matrix $\boldsymbol{\lambda}$ entirely describes the relative orientation of the two systems. The rotation matrix can be obtained by the following series of rotations (See Figure 5):

- The first rotation is anticlockwise through an angle ϕ about the c -axis, with the transformation matrix

$$\boldsymbol{\lambda}_\phi = \begin{pmatrix} \cos \phi & \sin \phi & 0 \\ -\sin \phi & \cos \phi & 0 \\ 0 & 0 & 1 \end{pmatrix} \quad (2.49)$$

- The second rotation is anticlockwise through an angle θ about the a' -axis, with its transformation matrix

$$\boldsymbol{\lambda}_\theta = \begin{pmatrix} 1 & 0 & 0 \\ 0 & \cos \theta & \sin \theta \\ 0 & -\sin \theta & \cos \theta \end{pmatrix} \quad (2.50)$$

- The third rotation is also anticlockwise through an angle ψ about c' -axis, with its transformation matrix

$$\lambda_\psi = \begin{pmatrix} \cos \psi & \sin \psi & 0 \\ -\sin \psi & \cos \psi & 0 \\ 0 & 0 & 1 \end{pmatrix} \quad (2.51)$$

- Finally, the new-rotated-coordinate system is evaluated by this equation

$$\mathbf{r}' = \lambda_\psi \lambda_\theta \lambda_\phi \mathbf{r}$$

$$\begin{pmatrix} x' \\ y' \\ z' \end{pmatrix} = \begin{pmatrix} \cos \psi & \sin \psi & 0 \\ -\sin \psi & \cos \psi & 0 \\ 0 & 0 & 1 \end{pmatrix} \begin{pmatrix} 1 & 0 & 0 \\ 0 & \cos \theta & \sin \theta \\ 0 & -\sin \theta & \cos \theta \end{pmatrix} \begin{pmatrix} \cos \phi & \sin \phi & 0 \\ -\sin \phi & \cos \phi & 0 \\ 0 & 0 & 1 \end{pmatrix} \begin{pmatrix} x \\ y \\ z \end{pmatrix} \quad (2.52)$$

In this work, the Eulerian angles method is applied in the FA cation-organic molecule in order to determine the energy landscapes corresponding to each orientation of the FA cation.

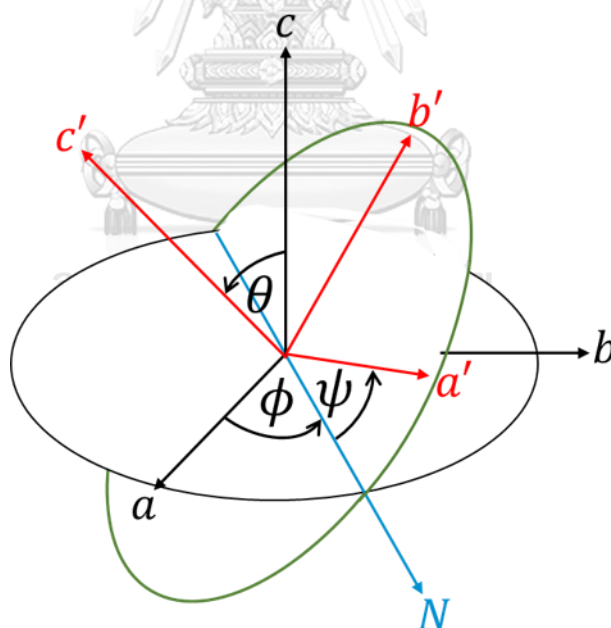


Figure 6: Eulerian angles geometrical definition. The fixed system is shown in black, the rotated system is shown in red. The nodal line (N) is shown in blue

3. CALCULATION DETAILS

In this work, the total energies accounting for each orientation of the FA cation were numerically calculated. The energy landscapes were to be presented, and the possible lowest energy orientation(s) is/are identified and used to evaluate the corresponding electronic band structures and density of states.

To make these processes possible, Quantum Espresso Package [40] had been used to investigate the physical properties of FAPI. The fully unconstrained noncollinear magnetism within the projector augmented wave method was used [41] to describe the core and valence electrons, the relaxation algorithm of atoms and lattice parameters used in this work is Broyden-Fletcher-Goldfarb-Shanno algorithm [37] with a force/atom tolerance equal to 0.001 Hartree/Bohr. The GGA method developed by Perdew-Burke-Ernzerhof (PBE) [42] has been selected. Since this system consists of *Pb* atoms, the spin-orbit coupling and fully relativistic effects are undeniably to be taken into account [43]. The spin-orbit coupling (SOC) [44] was applied to determine the total energy, optimised structures, and the density of states. To precisely evaluate physical quantities with the aid of DFT, the convergence test needs to be achieved systematically.

3.1 Convergence test of FAPI

The convergence tests are crucial in setting the limits of accuracy of the total ground –state energy of the system. The parameters needing to be varied are the kinetic cutoff energies and the k-point meshes. With both GGA functional, the conditions for the self-consistent field calculation are set to the total energy tolerance change of less than 6×10^{-6} Ry/atom, as the same value as of the calculated geometry optimisation.

The cubic structure of FAPI was optimised by the condition: the internal atoms are allowed to relax, while the shape and volume of 1737.1377 a.u.³ are kept fixed in order to be consistent with the experimentally reported value. There are two schemes of convergence test of FAPI. First, the k-point mesh of 4x4x4 was selected and kept as a fixed parameter, then the cutoff energies starting from 30 to 100 Ry were varied, and each of the calculated total energies corresponding to each of cutoff energies were then plotted in Figure 7, the energies abruptly decreases during the cutoffs from 30 to 70 Ry, the energies nearly maintain the same level of -2099.42 Ry, thus the

cutoff energy cutoff of 80 Ry was selected, since the more of other values give no difference in evaluating total energy of this system; the difference of cutoff energies between 80 and 90 Ry is 1.25×10^{-5} Ry or 0.17 meV, which is technically tolerable.

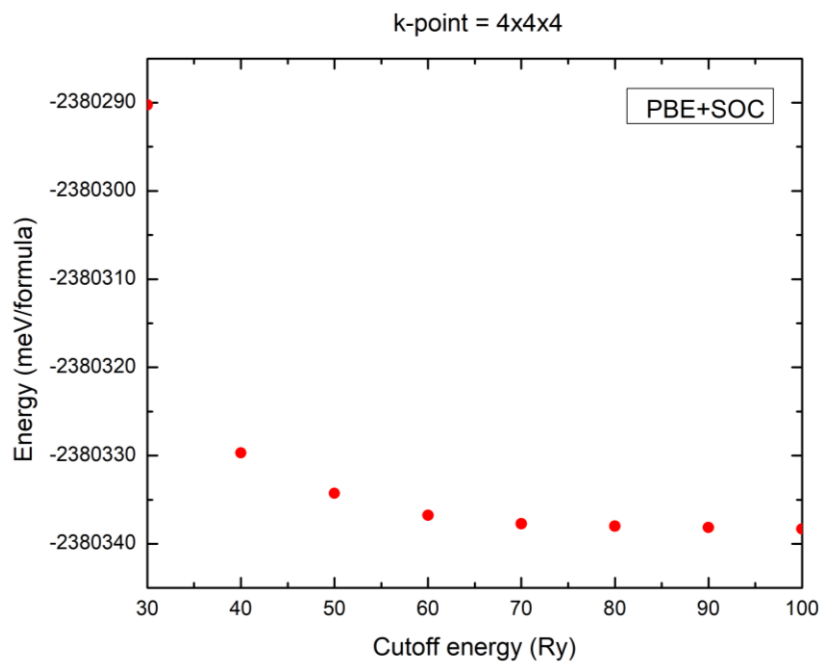


Figure 7: The relationship between the total energies and the cutoff energies when k-point is fixed at the value of 4x4x4

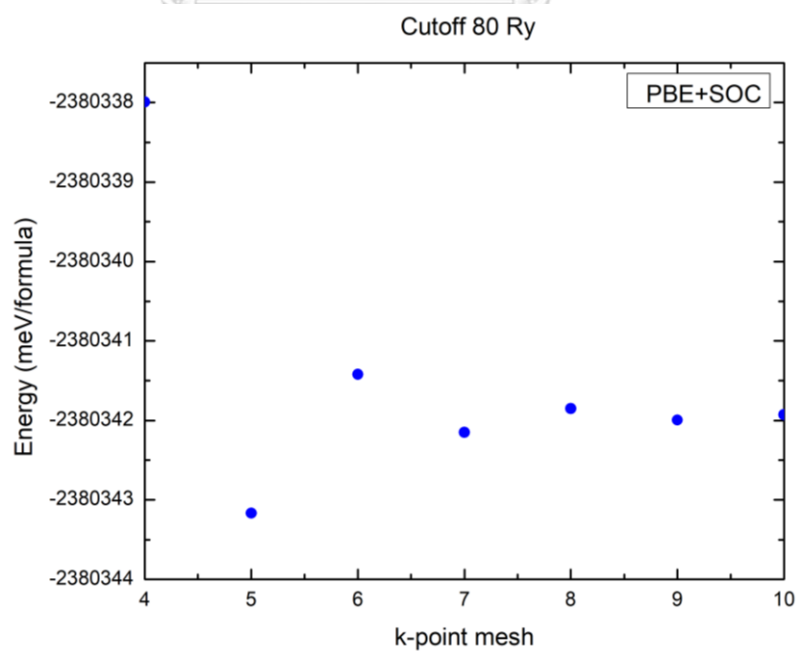


Figure 8: The relationship between the total energies and the k-point meshes when cutoff is fixed at the value of 80 Ry

Second, likewise, the cutoff energy of 80 Ry was selected and kept as a fixed parameter, then the k -point meshes starting from $4 \times 4 \times 4$ to $10 \times 10 \times 10$ were varied and plotted in Figure 8, the energy profile slightly fluctuates at first, but it tends to remain stable at $8 \times 8 \times 8$ onwards, the difference of energies between the k -point meshes of $8 \times 8 \times 8$ and $9 \times 9 \times 9$ is 1.0×10^{-5} Ry or **0.13 meV**, so thus the k -point mesh of $8 \times 8 \times 8$ was accordingly selected. Henceforth, the cutoff energy of 80 Ry and k -point mesh of $8 \times 8 \times 8$ were used as input parameters in calculating other physical properties of FAPI.

3.2 Relaxed structure of FAPI

As discussed in the previous section, the structure in the relaxation procedure with 80 Ry of cutoff energy and $8 \times 8 \times 8$ k -point mesh will be now called the “relaxed structure”, as depicted in Figure 5(b) and Figure 18 in Appendices, consisting of the slightly deviated I atoms, i.e. ~ 0.03 Å from their unrelaxed positions, and the slightly shifted FA molecule along the [100] direction. As a result, the inversion symmetry is already broken at this stage. This structure will be used as a starting point in the energy landscape calculation.

3.3 Euler’s rotation applied to relaxed cubic FAPI

In order to search for the lowest energy structure of FAPI, the FA cation has no choice but be reoriented through the Euler's rotation. As illustrated in Figure 9, the FA cation is planar lying in the (002) plane, and polar with its dipole parallel to the $C-H$ bond [45] (Blue arrow in Figure 9). In this work, the starting point was chosen such that the dipole moment direction points along the a -axis or [100] direction, denoted by the N -axis. Under rotation procedure, the centre of mass of the FA cation was set to be the origin of the body axes, so that the displacement of the rigid body—the FA cation—involves no translation of the body axes. Thus, the only change is in its orientation, and hence the corresponding internal displacements of the atoms in the FA cation according to the rotation about the body axes. The three Eulerian angles [46] are to rotate anti-clockwise. The definition of the Euler's rotation is as follows (see Figure 9(a)); ϕ is the angle between the N - and the a -axis (see Figure 9(b)), and θ is the angle between the b' - and the ab -plane (see Figure 9(c)), and ψ is the angle between the N - and the a' -axis (see Figure 9(d)). We explicitly set ($\phi = 0^\circ, \theta = 0^\circ, \psi = 0^\circ$) as the starting point.

Only in the range of $0^\circ - 90^\circ$ was preferred to rotate the FA cation through ϕ , θ and ψ . The flips of FA were discretised into 7 turning steps with a 15° step size for each angle of rotation, so that the sets of simulation contain 343 samples of orientations—covering a large area of two octants of the simulation cell. The remaining areas are just the repetition of nearly equivalent points in three dimensional space. After systematically applying the rigid flips to the FA cation, the energy calculation without structural relaxation was performed. The total energy of each orientation of the FA cation can be viewed as a function of ϕ , θ and ψ , i.e. $E \equiv E(\phi, \theta, \psi)$. The scattered data accumulated from the total energy calculations were interpolated adopting Renka-Cline gridding method [47] for plotting the energy landscape. However, it is worth mentioning that the order of the Eulerian angles cannot be interchanged. Consequently, the energy landscape plots can exactly be viewed as the plots between the energy and the corresponding FAPI configuration with the FA orientations specified by ϕ , θ and ψ rotations in orderly fashion.

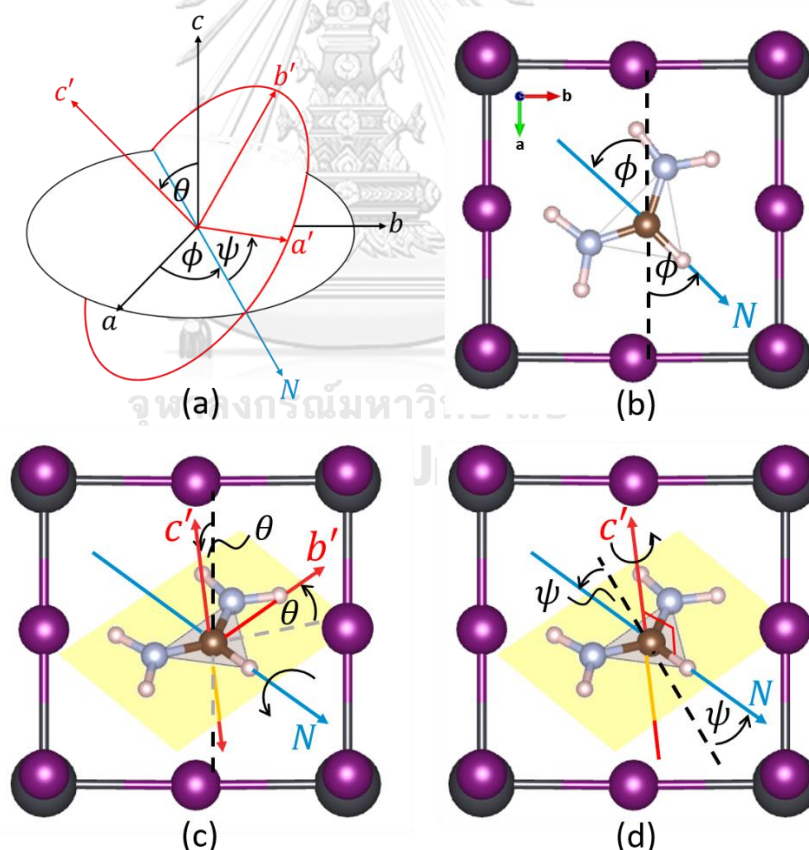


Figure 9: The corresponding Eulerian angles for the organic molecule of FA where C–H axis is directed to N–axis (a). First rotation is anti-clockwise through an angle ϕ about the c -axis (b). Second rotation is anti-clockwise through an angle θ about the a' -axis

4. RESULTS AND DISCUSSIONS

This section carefully describes all processes within this work as follows: First, we surveyed the energy landscape in the sample parameter space with $\phi = 0^\circ - 90^\circ$, $\theta = 0^\circ - 90^\circ$, and $\psi = 0^\circ - 90^\circ$, in order to search for the FA orientations having considerable potential for being the lowest energy configuration(s). After the candidates had already been found, the structural relaxation was then performed to guarantee that these orientations have the lowest possible energy. Then, the structural properties were analysed in terms of pair distribution function for bond-lengths. Finally, we performed the electronic calculation and reported the electronic band structures and the selections of the projected density of states.

4.1 Energy landscapes

As our simulations contain 343 samples of the FA cation's orientations—covering two octants of the simulation cell, one can construct the energy as a function of orientation parameters specified by (ϕ, θ, ψ) . For simplicity, it is reported here some cross section of $E(\phi, \theta, \psi)$. The cross section through $\psi = 0^\circ$ is a quintessential interpretation, thus one can present $E(\phi = 0^\circ - 90^\circ, \theta = 0^\circ - 90^\circ, \psi = 0^\circ)$ in a three dimensional (3D) plot, as shown in Figure 10. In this saddle-like landscape, there are a few special paths in this 3D plot which represent the so-called single axis rotation. It is worth considering that the path with the FA cation oriented via $(\phi = 0^\circ - 90^\circ, \theta = 0^\circ, \psi = 0^\circ)$ simply represents the rotation about the C -axis. Quintessentially, the energy along this transition path resembles a Gaussian-like barrier, with the barrier height of 17 meV.

Table 1: Some energies calculated for ϕ , θ and ψ , relative to FAPI with $(90^\circ, 60^\circ, 45^\circ)$ -FA.

ϕ (°)	θ (°)	ψ (°)	E-E ₀ (meV)
0	0	0	7.63
90	15	0	8.10
90	75	0	7.34
45	60	45	0

A similar calculation was performed by Fabini *et al.* [48], who reported the barrier height of 21 meV along a similar path. The discrepancy arises from the fact that we do not perform further

structure relaxation at this stage. Another path is along $(\phi = 90^\circ, \theta = 0^\circ, \psi = 0^\circ)$ which represents the rotation about the N -axis. The energy barrier along this path is as low as 2.5 meV. Thus the FA cation can easily flip along this path, despite at very low temperature. Here, we reported also some selected points in the energy landscapes in Table 1 in comparison with the results reported by Fabini *et al.* [48].

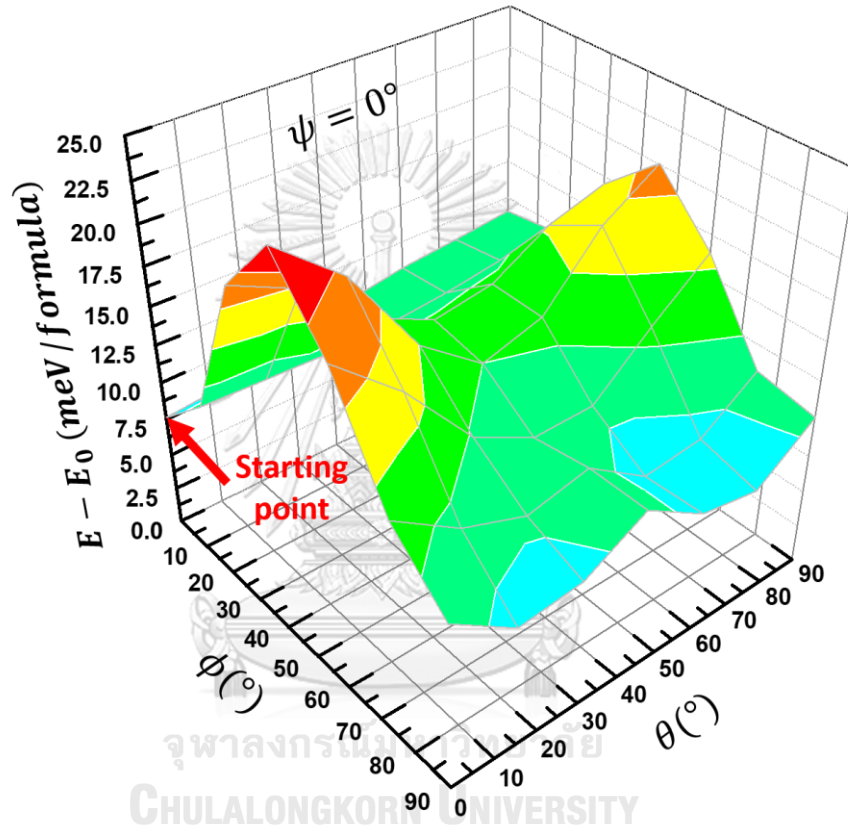


Figure 10: The total energy profile as a function of ϕ , θ , and $\psi = 0^\circ$, taking the lowest total energy as a reference. The scattered data are interpolated adopting Renka-Cline gridding method [47]. The starting point is responsible for $(0^\circ, 0^\circ, 0^\circ)$ configuration.

The energy barriers can be interpreted as entities, to some extent, intertwining with thermal agitation, i.e. $\Delta E \sim k_B T$, where ΔE indicates any flipping energy barrier. It was found that the highest barrier of all sets of rotations is of 24.7 meV (see Figure 20 in the Appendices), which is corresponding to $T = 286$ K of thermal excitation energy. This means that at temperature higher than 286 K, the FA cation is able to freely and randomly rotate to any values of ϕ , θ and ψ .

Another important consideration is the cross section cutting through $\psi = 45^\circ$. We present $E(\phi = 0^\circ - 90^\circ, \theta = 0^\circ - 90^\circ, \psi = 45^\circ)$ in the 3D plot, as shown in Figure 11. As for the $(90^\circ, 60^\circ, 45^\circ)$ –FA orientation landscape, it is found to be the lowest possible energy structure (see Point A in Figure 11 and Figure 27 in Appendices for the energy and Figure 12 for the structure). Consequently, this configuration was taken and performed further structure relaxation. The result suggests that its energy is the lowest possible and the final structure changes slightly, see Figure 19 in the Appendices. The Pb and I atoms slightly shift, and the $I3 - Pb - I3$ angle is reduced by $\sim 7^\circ$, but FAPI remains a cubic structure. Our lowest energy structure, the $(90^\circ, 60^\circ, 45^\circ)$ configuration, is in contrast with the $(0^\circ, 0^\circ, 0^\circ)$ configuration previously suggested by Weller *et al* [19].

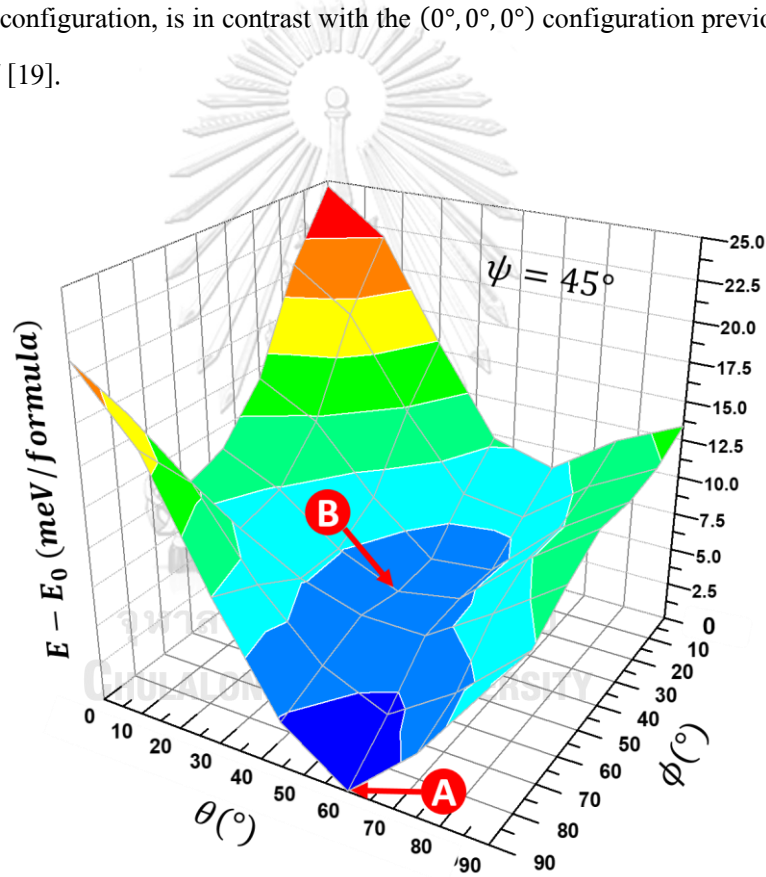


Figure 11: The total energy profile as a function of ϕ , θ , and $\psi = 45^\circ$, taking the lowest energy as a reference (point A). The scattered data are also interpolated adopting Renka-Cline gridding method [47]. The next higher energy (point B) is responsible for the equivalent lowest energy configuration.

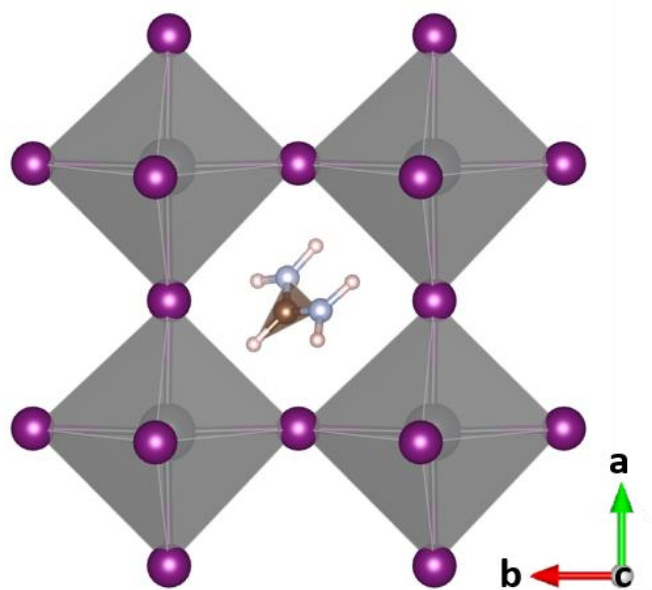


Figure 12: The optimum structure of FAPI with the FA cation orienting along ($\phi = 90^\circ, \theta = 60^\circ, \psi = 45^\circ$) direction.

4.2 Pair distribution function for bond-lengths of three structures of FAPI

The distribution of distances between pairs of particles, in this case the bond lengths of $H-I$ bonds, contained within a given volume can be described by the pair distribution function (PDF) [49]. One can determine the PDF by calculating the bond lengths of all pairs of $H-I$ and binning them into a histogram.

As for further analysis on the structure properties of the $(0^\circ, 0^\circ, 0^\circ)$ and $(90^\circ, 60^\circ, 45^\circ)$ configurations, as depicted in Figure 13, Table 5 and 6 in the Appendices, we found that the $I-H$ pair distribution of the unrelaxed and $(0^\circ, 0^\circ, 0^\circ)$ configuration can be roughly divided into three shells as follows: 2.75–3.20 Å, 3.40–4.20 Å and around 4.70 Å (orange and turquoise bars in Figure 13). The $I-H$ pair distribution, of the $(90^\circ, 60^\circ, 45^\circ)$ configuration, on the other hand, can be divided into only two shells as follows: 2.75–3.20 Å and 3.40–4.20 Å (purple bars in Figure 13). It can be interpreted that the lowest energy structure has the optimum bond-lengths between the I and H atoms. There will be soon an explanation on a weak interaction between the FA cation and the PbI_6 framework.

In the perfect cubic structure, the positions of the I atoms, i.e. I_1 , I_2 , and I_3 , are exactly equivalent in terms of spatial symmetry. Therefore, the organic molecule would not be restricted

to arrange itself just only in the preferred orientation, $(90^\circ, 60^\circ, 45^\circ)$. Rather it must have a multiple of three equivalent sites. We found that Point B in Figure 11 is an example of these equivalent configurations. Even though the point B appears to have higher energy in Figure 11, after relaxation process, it falls into the lower energy state, and its structure becomes equivalent to that of the $(90^\circ, 60^\circ, 45^\circ)$ configuration. These different orientations of the FA cation, together with the corresponding displacements of the *Pb* and *I* atoms, directly lead to the inversion symmetry breaking in *PbI₆*, the inorganic framework. Consequently, this structural asymmetry will be responsible for the change in the electronic property, *vide infra*.

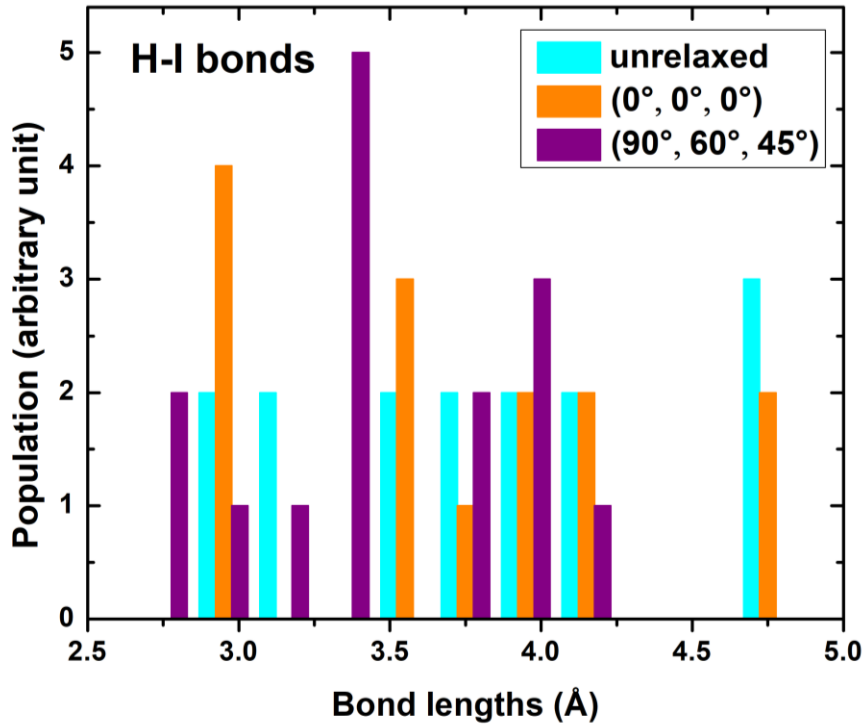


Figure 13: The pair distribution of H-I bonds for three FAPI structures, i.e. unrelaxed, $(0^\circ, 0^\circ, 0^\circ)$, and $(90^\circ, 60^\circ, 45^\circ)$ configurations, respectively.

4.3 Electronic band structures

It was reported in the case of MAPI that the conduction band minimum (CBM) stems from the *Pb(6p)*-*I(5p)* anti-bonding states, whereas the valence band maximum (VBM) is brought about by the *Pb(6p)*-*I(5p)* bonding and the *I(5p)* non-bonding states. In addition, the VBM is mostly dominated by the *I(5p)* lone pair states [50]. These features are similar to the case of FAPI

as well. In our unrelaxed α -FAPI unit cell, there are three equivalent sites for the I atoms in the perfect $Pm\bar{3}m$ space group. As a consequence, the density of states responsible for those three $I(5p)$ lone pairs are degenerate. Surprisingly, the bandgap from the sole PBE calculation (1.44 eV) is fortuitously close to the experimental reported value, i.e. 1.41 eV [17]. While performing the SOC calculation, we nevertheless found that the CBM band is splitting due to the strong SOC effect on the $Pb(6p)$ states. The position of the CBM is lowered down and the electronic bandgap is narrowing [51]. A similar feature was reported by Mosconi *et al.* in MAPI [52]. But the bandgaps can accurately be corrected by including the effects of the strongly correlated electrons which can be achieved by using the GW method or the hybrid functionals [51, 53, 54].

The effect of the orientations of the FA molecule on the electronic structure was carefully and systematically inspected. Figures 14 and 15 exhibit the electronic structures along the selected high-symmetry points in the first Brillouin zone of the relaxed $(0^\circ, 0^\circ, 0^\circ)$ and $(90^\circ, 60^\circ, 45^\circ)$ configurations, respectively. The energy gaps of the $(0^\circ, 0^\circ, 0^\circ)$ and the $(90^\circ, 60^\circ, 45^\circ)$ configurations read 0.15 and 0.28 eV, respectively, compared with the experimentally reported value of 1.41 eV [17]. The discrepancies are explained due to the strongly correlated nature of the electrons: PBE+SOC removes degeneracies [17, 55] from PBE, generally underestimates bandgaps (for further discussion of this issue, see Perdew [56] *et passim*, thanks to the spin-orbit coupling (SOC) effect which largely stemmed from the Pb atoms. The tendency of the SOC splitting reduces the bandgap by about 1 eV. Strictly speaking, if one compare the bandgap of 1.44 eV, from the PBE calculation, with the bandgap of 0.28 eV obtained from the PBE+SOC calculation of the $(90^\circ, 60^\circ, 45^\circ)$ configuration, the difference is of order of 1 eV.

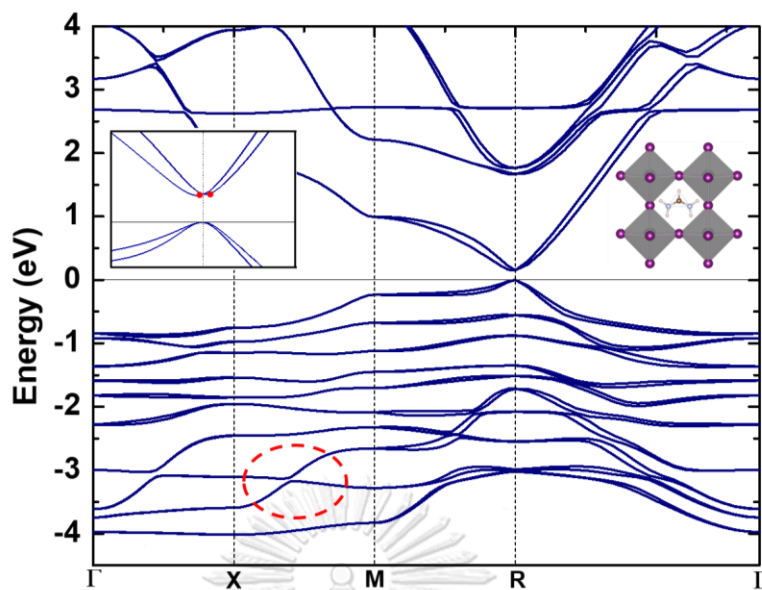


Figure 14: The electronic band structure of the relaxed FAPI with relaxed $(0^\circ, 0^\circ, 0^\circ)$ -FA molecule. The dashed circle reveals weak interaction between the I atom and the PbI_6 framework.

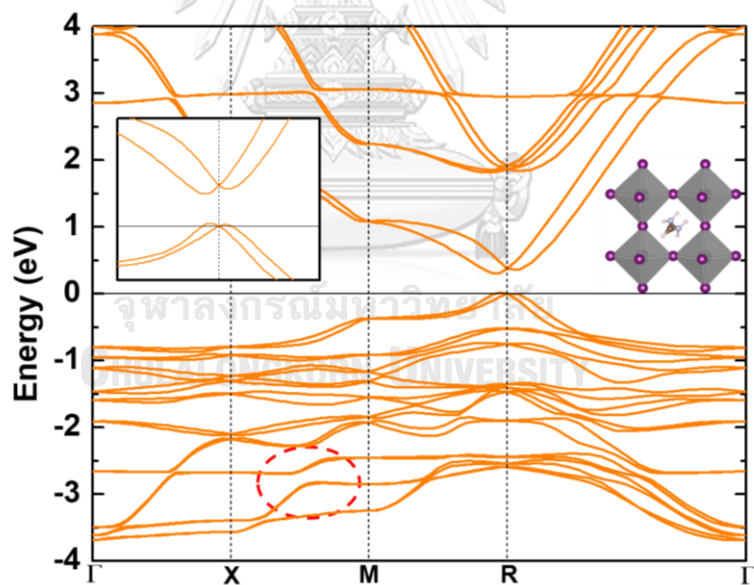


Figure 15: The electronic band structure of the relaxed FAPI with $(90^\circ, 60^\circ, 45^\circ)$ -FA. In the same manner, the dashed circle reveals weak interaction between the I atom and the PbI_6 framework.

4.4 Projected density of states

The effects of the FA cation on the inorganic cage is further verified by calculating the projected density of states (pDOS), as shown in Figures 16 (a and b). As mentioned above, there exists the non-bonding $I(5p)$ orbitals of the $I1$, $I2$ and $I3$ atoms in the valence states. In the unrelaxed configuration scheme, these three states are theoretically degenerate, i.e. the branches never split. However, upon the FA molecular rotation, the inversion symmetry of cubic FAPI is broken. Consequently, the $I1$, $I2$, and $I3$ atoms become clearly distinguishable, and the corresponding electronic bands are splitting. The pDOS of the $(0^\circ, 0^\circ, 0^\circ)$ configuration are shown in Figure 14. The three highest peaks near the Fermi level are those of the distinguishable $I1$, $I2$, and $I3$ atoms. It is worth mentioning that one of the three peaks is out of alignment (brown) and the position of the peak is at lower energy compared with the other two, pointed by red arrow the Figure 16(a). This causes the $(0^\circ, 0^\circ, 0^\circ)$ configuration to dwell in a slightly lower energy state, compared with the unrelaxed configuration.

The pDOS of the $(90^\circ, 60^\circ, 45^\circ)$ configuration are shown in Figure 16(b). Again, the three highest peaks near the Fermi level are those of the distinguishable $I1$, $I2$, and $I3$ atoms. These three peaks shift towards lower energies in a similar manner, thus the $(90^\circ, 60^\circ, 45^\circ)$ configuration possesses the relatively lowest possible energy. As these I non-bonding states are dominating the VBM, we also found that the bandgap in this configuration is widened slightly to be 0.28 eV, compared with 0.15 eV of the $(0^\circ, 0^\circ, 0^\circ)$ configuration.

The unfavourable states corresponding to the non-bonding p -orbitals of the I atoms of the PbI_6 inorganic framework are likely to adjust themselves to dwell in a more stable configuration by deviating the $I3-Pb-I3$ angles of the $(0^\circ, 0^\circ, 0^\circ)$ and the $(90^\circ, 60^\circ, 45^\circ)$ configurations to be less than 180° , i.e. around 173° and 167° , respectively, leading to the so-called octahedral tilting. The investigation of octahedral tilting in MAPI was thoroughly carried out and discussed by J. H. Lee *et al* [50].

In addition, Figures 14 and 15 also show a couple of nearly non-dispersive bands in the valence and the conduction bands, which can be assigned to the FA molecule. The dashed circles reveal the weak interaction between the FA cation and the PbI_6 inorganic framework. The interaction is a little stronger in the $(90^\circ, 60^\circ, 45^\circ)$ configuration. Apart from this weak interaction, the FA cation seems to only exert strain onto the PbI_6 cage, leading to the structural asymmetry

which eventually leads to the Rashba splitting effect, as will be discussed next. These aforementioned results are similar to a previous work on MAPI which suggested that MAPI is a dynamical bandgap semiconductor [21].

The most important effect of our specific orientations of the FA molecule is to remove the inversion symmetry. The perovskite structure already becomes non-centrosymmetric. This symmetry breaking regime has a crucial impact on the electronic structure. Apart from the vertical SOC splitting, the electronic band also exhibits an exotic horizontal spin-splitting phenomena [57], the Rashba/Dresselhaus effect [45], as zoomed in the inset of Figures 14 and 15. For the $(0^\circ, 0^\circ, 0^\circ)$ configuration, the Rashba splitting in the conduction band minimum is at around $R \pm 0.01$ (see Figure 14 and the inset). For the $(90^\circ, 60^\circ, 45^\circ)$ configuration, the Rashba splitting in conduction band minimum is at around $R \pm 0.025$ (see Figure 5 and the inset). From these R -points, the Rashba parameters can be evaluated by calculating $2\alpha = \Delta\epsilon/\Delta k$ [58]. For the $(90^\circ, 60^\circ, 45^\circ)$ configuration, along the $R \rightarrow M$ branch, the Rashba parameters are responsible for $\alpha_C \sim 3.0$ and $\alpha_V \sim 1.4$ of the CBM and VBM, respectively, and along the $R \rightarrow \Gamma$ branch, $\alpha_C \sim 2.3$ and $\alpha_V \sim 1.4$ for the CBM and VBM, respectively. For comparison, MAPI also exhibits the Rashba splitting and $\alpha \sim 2$ as reported by Mosconi *et al* [58].

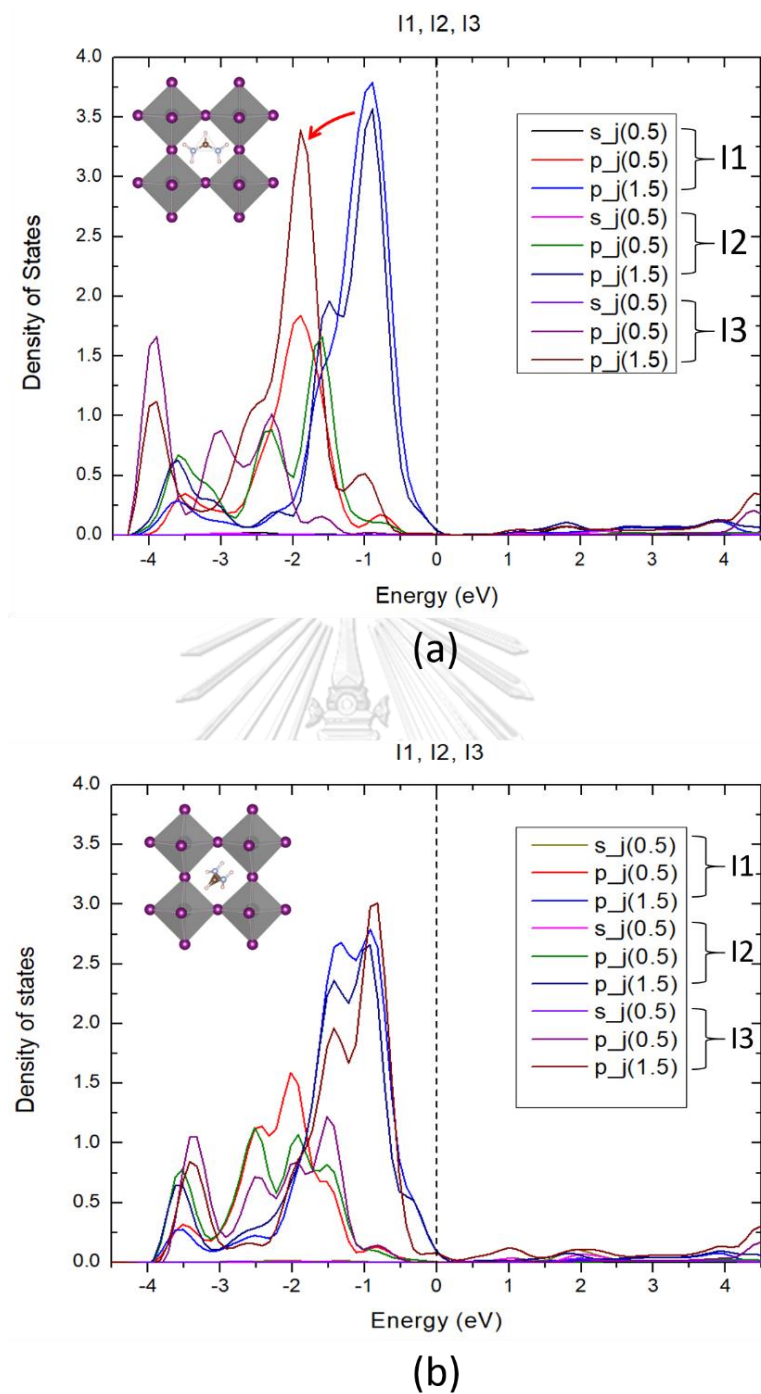


Figure 16: The projected-density of states for the relaxed FAPI. The relaxed structure with relaxed (0°, 0°, 0°) oriented FA with a peak of I3 shifting leftwards compared to that of the perfect cubic FAPI (a). The corresponding FAPI with (90°, 60°, 45°)-FA (b).

5. CONCLUSION

Effects of the organic molecules of formamidinium (FA) on $FAPbI_3$ are thoroughly and systematically inspected. Equipped with Euler's rotation, the mechanistic explanations of both the structural and electronic properties of this system emerge unexpectedly. The perfect cubic structure of FAPI had first been optimised to possess the optimal energy structure. The agreeable values of kinetic energy cutoff and k -point mesh as the selected products from the convergence tests were hereafter used throughout all processes of calculation. Then, the relaxed structure was kept fixed except for the organic molecule in order to be applied a rigid turn based on Eulerian angles to verify its energies accounting for different orientations of the FA cation. Crucially, the energy landscapes responsible for different orientations of the organic molecule were studied and turned out that the relatively lowest energy structure of FAPI happens to consist of FA cation oriented in $(\phi = 90^\circ, \theta = 60^\circ, \psi = 45^\circ)$ direction and its equivalent orientations. The flipping energy barriers were interpreted to be thermal agitations required for FA to turn to other orientations. As a consequence, the electronic band structures of two cases, i.e. FAPI with $(0^\circ, 0^\circ, 0^\circ)$ -FA and that with $(90^\circ, 60^\circ, 45^\circ)$ -FA display various types of phenomena. Specifically, the latter one exhibits an interesting result, i.e. the well-known Rashba-Dresselhaus effect originating from concurrent appearance of spin-orbit interaction and inversion symmetry breaking in crystal structure. As for the future work, various types of organic molecules dwelling in the perovskite structure are to be studied. Not only do their structural and electronic properties, but also do their optical response that leads to industrialisation. Finally, we suggest that a possible way for engineering the band-edge tunable FAPI is to exploit its temperature dependence. Not only may these discoveries possibly enhance the utilisation of this material in the memory and data storage industries, but also vivid potential candidate for optoelectronic applications.

APPENDICES

A. Energy minimisation

The ground-state energy can be achieved by adopting variational principle, specifically Euler's equation with a separate Lagrange multiplier (λ_i), which is written as

$$\frac{\delta}{\delta n(\mathbf{r})} \left[\varepsilon[n(\mathbf{r})] - \sum_i^N \lambda_i \int n(\mathbf{r}) d\mathbf{r} \right] = 0 \quad (\text{A.1})$$

Due to the normality constraint of each orbital, the number of electrons must be conserved,

$$\sum_i^N \int \Psi_i^{*KS}(\mathbf{r}) \Psi_i^{KS}(\mathbf{r}) d\mathbf{r} = N, \quad (\text{A.2})$$

Recall the total energy functional:

$$\varepsilon[n(\mathbf{r})] = T_0[n(\mathbf{r})] + \frac{1}{2} \int \int \frac{n(\mathbf{r}) n(\mathbf{r}')}{|\mathbf{r} - \mathbf{r}'|} d\mathbf{r} d\mathbf{r}' + \int V_{ext}(\mathbf{r}) n(\mathbf{r}) d\mathbf{r} + E_{xc}[n(\mathbf{r})], \quad (\text{A.3})$$

where $T_0[n(\mathbf{r})]$ is defined as the kinetic energy of the non-interacting electron gas with density $n(\mathbf{r})$,

$$T_0[n(\mathbf{r})] = \sum_i^N \int \Psi_i^{*KS}(\mathbf{r}) \left(-\frac{\nabla^2}{2} \right) \Psi_i^{KS}(\mathbf{r}) d\mathbf{r}. \quad (\text{A.4})$$

According to Liu *et al.* [59], a rigorous proof of derivative of $T_0[n(\mathbf{r})]$ was discussed in detail.

Thus we have

$$\frac{\delta T_0[n(\mathbf{r})]}{\delta n(\mathbf{r})} + V_{eff}(\mathbf{r}) = \lambda, \quad (\text{A.5})$$

where

$$V_{eff}(\mathbf{r}) = V_{ext}(\mathbf{r}) + \int \frac{n(\mathbf{r}')}{|\mathbf{r} - \mathbf{r}'|} d\mathbf{r}' + V_{xc}, \quad (\text{A.6})$$

and the exchange-correlation potential is written as

$$V_{xc}(\mathbf{r}) = \frac{\delta E_{xc}[n(\mathbf{r})]}{\delta n(\mathbf{r})}. \quad (\text{A.7})$$

Eq. (A.5) with the constraint (A.2) is exactly the same equation as one obtains from DFT when one applies it to a system of non-interacting electrons moving in the external potential $V_{eff}(\mathbf{r})$.

Therefore, we can write Eq. (A.5) as

$$\frac{1}{\Psi_i^{*KS}(\mathbf{r})} \frac{\delta T_0[n(\mathbf{r})]}{\delta \Psi_i^{KS}(\mathbf{r})} + V_{eff}(\mathbf{r}) = \lambda, \quad (\text{A.8})$$

Finally, to solve for the ground –state energy and density, all one has to do is solve the one-electron equation,

$$\left[-\frac{\nabla_i^2}{2} + V_{eff}(\mathbf{r}) \right] \Psi_i^{KS}(\mathbf{r}) = \varepsilon \Psi_i^{KS}(\mathbf{r}). \quad (\text{A.9})$$

B. Euler's method for the Hartree energy

Given the Hartree energy as,

$$J[n(\mathbf{r})] = \frac{1}{2} \iint \frac{n(\mathbf{r})n(\mathbf{r}')}{|\mathbf{r} - \mathbf{r}'|} d\mathbf{r}d\mathbf{r}'. \quad (\text{A.10})$$

According to variational principle, one can implement Eq. (A.11) in order to obtain the Hartree potential. The functional derivative of any functional, $J[n(\mathbf{r})]$, is defined by Eq. (A.11), where $\phi(\mathbf{r})$ is an arbitrary function.

$$\int \frac{\delta J[n(\mathbf{r})]}{\delta n(\mathbf{r})} \phi(\mathbf{r}) d\mathbf{r} = \left[\frac{d}{d\varepsilon} J[n(\mathbf{r}) + \varepsilon \phi(\mathbf{r})] \right]_{\varepsilon=0} \quad (\text{A.11})$$

$$\equiv \left[\frac{d}{d\varepsilon} \frac{1}{2} \iint \frac{[n(\mathbf{r}) + \varepsilon \phi(\mathbf{r})][n(\mathbf{r}') + \varepsilon \phi(\mathbf{r}')] }{|\mathbf{r} - \mathbf{r}'|} d\mathbf{r}d\mathbf{r}' \right]_{\varepsilon=0} \quad (\text{A.12})$$

$$= \frac{1}{2} \iint \frac{[n(\mathbf{r}')\phi(\mathbf{r})]}{|\mathbf{r} - \mathbf{r}'|} d\mathbf{r}d\mathbf{r}' + \frac{1}{2} \iint \frac{[n(\mathbf{r})\phi(\mathbf{r}')] }{|\mathbf{r} - \mathbf{r}'|} d\mathbf{r}d\mathbf{r}' \quad (\text{A.13})$$

Since \mathbf{r} and \mathbf{r}' are interchangeable, thus the two integrands are equal. As a result, the variation of the Hartree energy is expressed as

$$\frac{\delta J[n(\mathbf{r})]}{\delta n(\mathbf{r})} = \int \frac{n(\mathbf{r}')}{|\mathbf{r} - \mathbf{r}'|} d\mathbf{r}'. \quad (\text{A.14})$$

C. Atomic coordinates of the input structure of FAPI

- 1) The cubic structure of $HC(NH_2)_2PbI_3$ or FAPI [19] with a lattice parameter of 3.3613 Å consists of atoms as described in Table 2 and depicted in Figure 16.
- 2) The relaxed structure of FAPI with a lattice parameter of 3.3613 Å consists of atoms as described in Table 3 and depicted in Figure 17.
- 3) The lowest energy structure of FAPI with a lattice parameter of 3.3613 Å consists of atoms as described in Table 4 and depicted in Figure 18.

Table 2: Atomic fractional coordinates of FAPI

Atoms	x	y	z
C	0.569011	0.500000	0.500000
N1	0.475280	0.682927	0.500000
N2	0.475280	0.317071	0.500000
H1	0.741416	0.500000	0.500000
H2	0.814009	0.567630	0.500000
H3	0.315280	0.704462	0.500000
H4	0.315280	0.295538	0.500000
H5	0.567630	0.185991	0.500000
Pb	0.000000	0.000000	0.000000
I1	0.000000	0.500000	0.000000
I2	0.500000	0.000000	0.000000
I3	0.000000	0.000000	0.500000

Table 3: Atomic fractional coordinates of relaxed FAPI with (0°, 0°, 0°)-FA

Atoms	x	y	z
C	0.572103	0.4997166	0.500000
N1	0.478304	0.682889	0.500000
N2	0.478309	0.316526	0.500000
H1	0.743669	0.500131	0.500000

Atoms	x	y	z
H2	0.570939	0.813387	0.500000
H3	0.319234	0.703188	0.500000
H4	0.319128	0.296325	0.500000
H5	0.571127	0.186119	0.500000
Pb	0.001372	0.000009	0.000000
I1	0.005391	0.499948	0.000000
I2	0.493962	-0.000113	0.000000
I3	-0.029541	-0.000127	0.500000

Table 4: Atomic fractional coordinates of relaxed FAPI with (90°, 60°, 45°)-FA

Atoms	x	y	z
C	0.454035	0.546184	0.500231
N1	0.460160	0.416006	0.340906
N2	0.583702	0.540707	0.660055
H1	0.332394	0.667728	0.499895
H2	0.348420	0.427592	0.225528
H3	0.566894	0.296596	0.331098
H4	0.703094	0.434121	0.670797
H5	0.571145	0.652515	0.775273
Pb	0.001541	-0.005318	0.999580
I1	0.014478	0.499174	0.008818
I2	0.497450	-0.013184	0.989476
I3	-0.037545	0.038506	0.498344

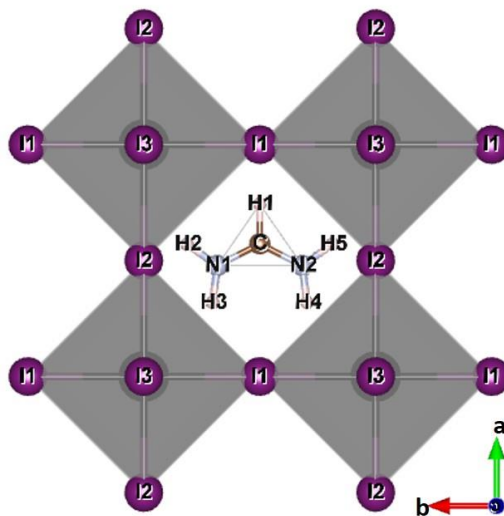


Figure 17: α -FAPI

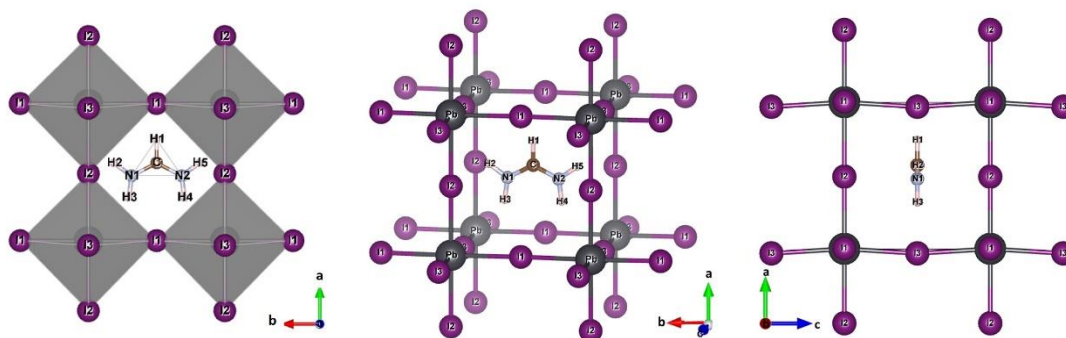


Figure 18: relaxed α -FAPI with $(0^\circ, 0^\circ, 0^\circ)$ -FA

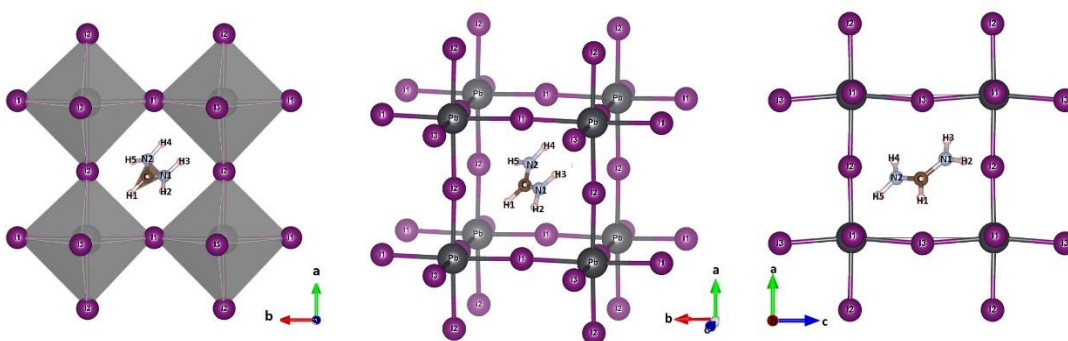


Figure 19: relaxed α -FAPI with $(90^\circ, 60^\circ, 45^\circ)$ -FA

D. Energy landscapes

Energy landscapes are scatter-plotted in three-dimensional space, where the scattered data were interpolated adopting Renka-Cline gridding method [47]. The energy landscapes with fixed ϕ -angle are plotted in Figures 20-26.

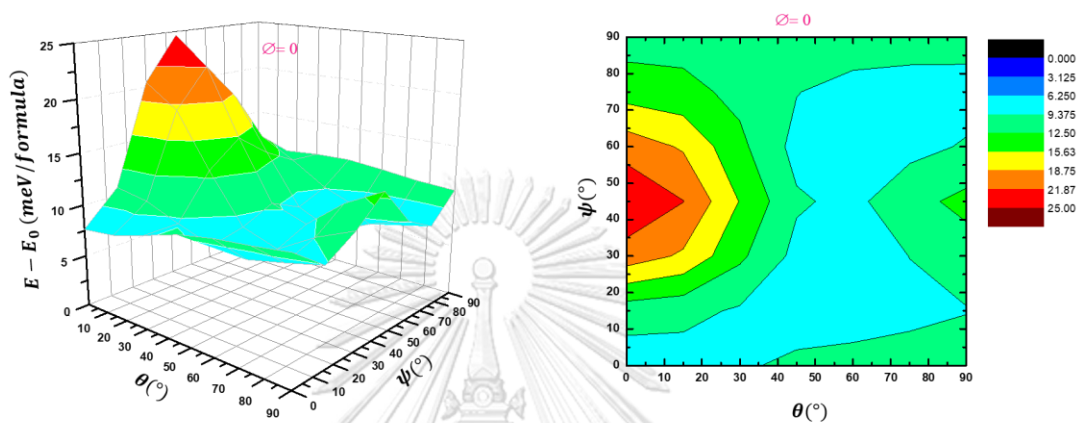


Figure 20: Energy landscape of $(\phi = 0^\circ, \theta, \psi)$ -FA

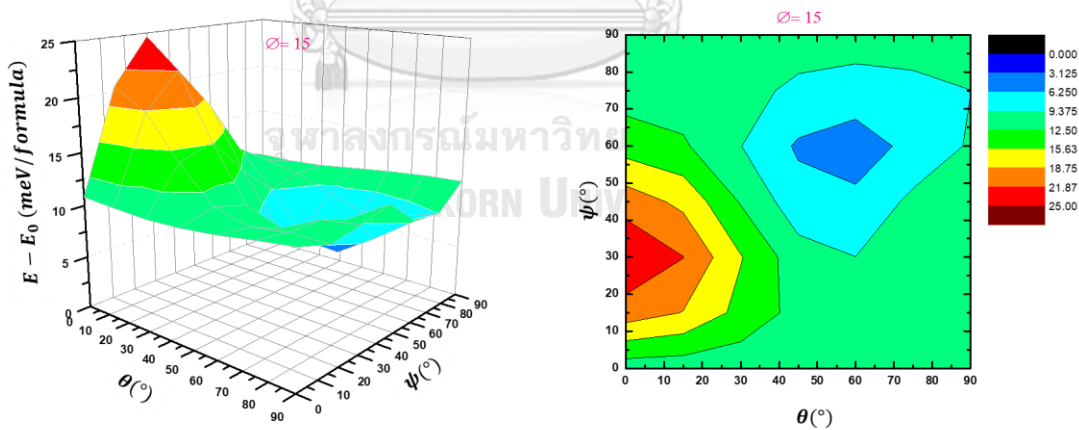


Figure 21: Energy landscape of $(\phi = 15^\circ, \theta, \psi)$ -FA

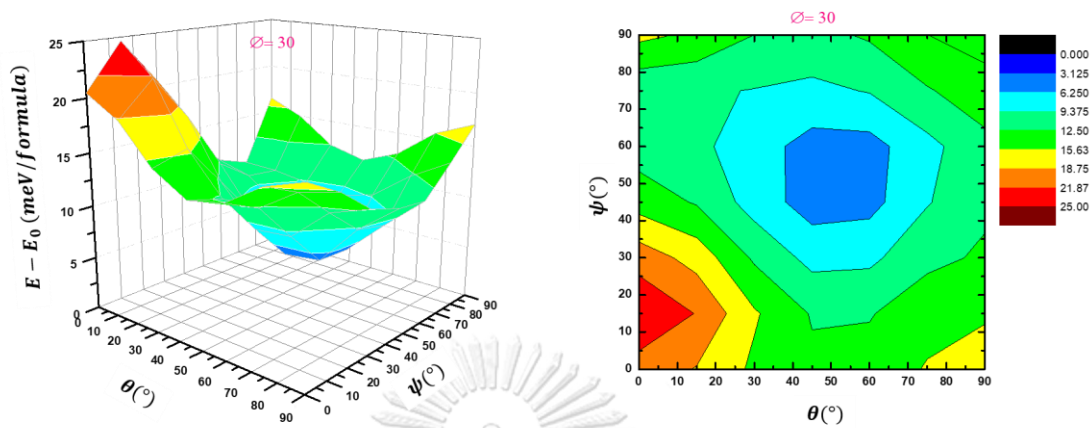


Figure 22: Energy landscape of $(\phi = 30^\circ, \theta, \psi)$ -FA

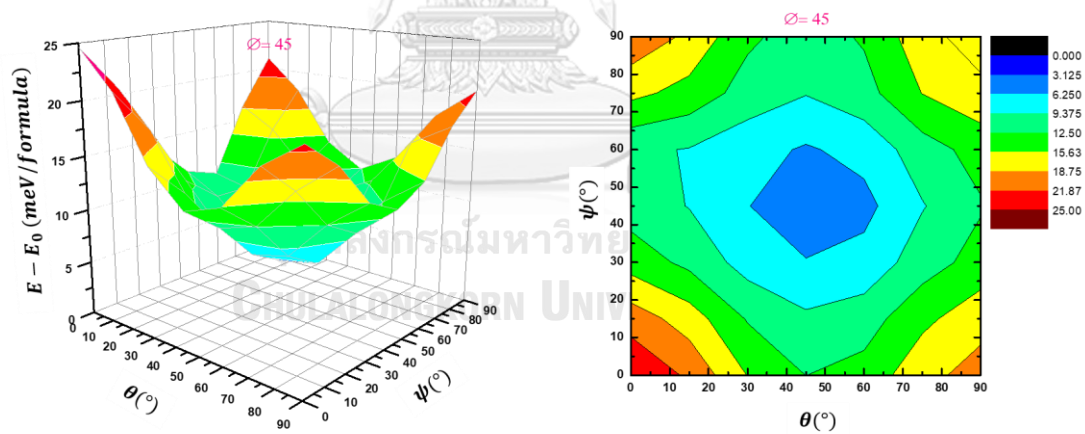


Figure 23: Energy landscape of $(\phi = 45^\circ, \theta, \psi)$ -FA

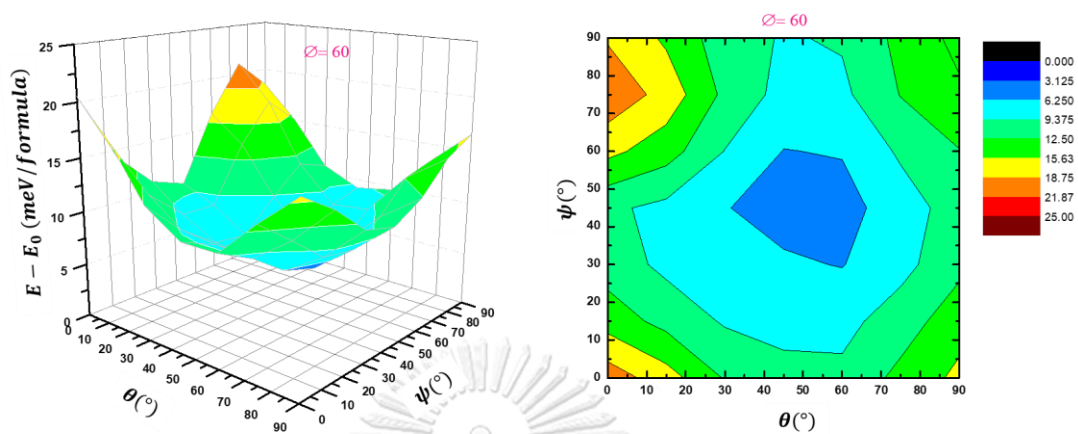


Figure 24: Energy landscape of $(\phi = 60^\circ, \theta, \psi)$ -FA

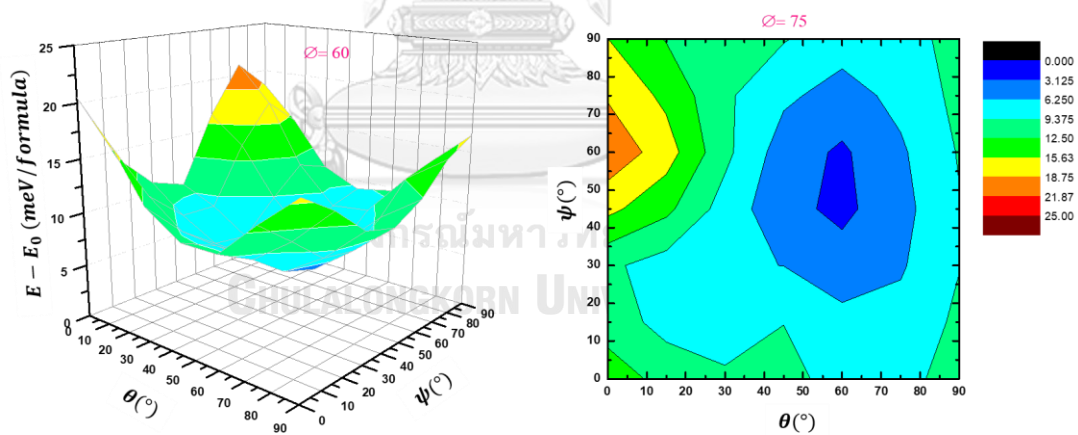


Figure 25: Energy landscape of $(\phi = 75^\circ, \theta, \psi)$ -FA

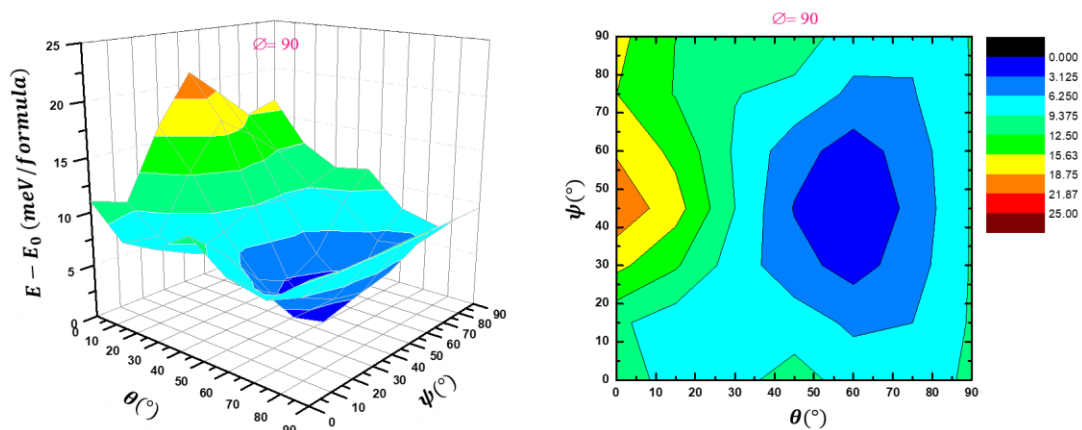


Figure 26: Energy landscape of $(\phi = 90^\circ, \theta, \psi)$ –FA

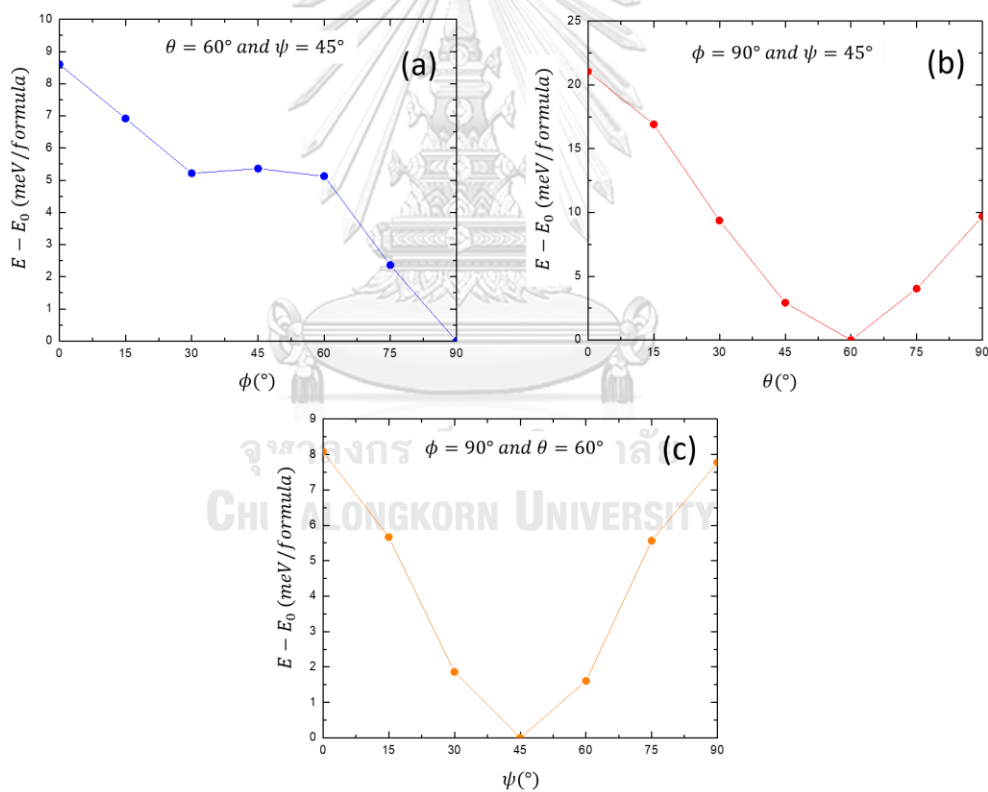


Figure 27: The energy landscape cross section of the $(90^\circ, 60^\circ, 45^\circ)$ –FA configuration.

E. Equivalent configurations

The relaxed structures of three configurations possessing nearly the same value of total energies are described in Table 5. The equivalent results from the fact that $C-H$ bond is likely to point to I atoms: $I1$, $I2$, $I3$.

Table 5: The bond-lengths of three different structures of FAPI: unrelaxed structure, (0°, 0°, 0°)–FA structure, and (90°, 60°, 45°)–FA structure.

Types of bonding	Unrelaxed (Å)	(0°, 0°, 0°)–FA (Å)	(90°, 60°, 45°)–FA (Å)
<i>Pb–I1</i>	3.18	3.18	3.15
<i>Pb–I2</i>	3.18	3.13	3.15
<i>Pb–I3</i>	3.18	3.18	3.19
<i>I1–H1</i>	3.57	3.59	3.87, 3.96
<i>I1–H2</i>	4.64, 5.22	4.66, 5.19	2.57
<i>I1–H3</i>	3.98, 5.52	3.97, 5.55	3.73, 4.27
<i>I1–H4</i>	3.98, 5.22	3.97, 5.55	2.95, 4.67
<i>I1–H5</i>	4.64, 5.22	4.66, 5.20	3.33, 3.96
<i>I2–H1</i>	4.75	4.77, 4.77	3.97, 3.86
<i>I2–H2</i>	3.42	3.43	3.32, 3.97
<i>I2–H3</i>	3.87	3.86	2.96, 4.65
<i>I2–H4</i>	3.87	3.86	3.73, 4.26
<i>I2–H5</i>	3.42	3.43	2.57
<i>I3–H1</i>	3.57	3.49	3.33
<i>I3–H2</i>	2.98	2.80	3.89
<i>I3–H3</i>	2.77	2.91	3.19
<i>I3–H4</i>	2.77	2.91	3.20
<i>I3–H5</i>	2.97	2.80	3.92

Table 6: Some possible lowest energy relaxed configurations of FAPI

Bond-lengths	(90°, 60°, 45°)-FA	(30°, 60°, 45°)-FA
<i>Pb-I1</i>	3.15	3.19
<i>Pb-I2</i>	3.15	3.17
<i>Pb-I3</i>	3.21	3.20
<i>I1-H1</i>	3.87, 3.96	3.80, 4.06
<i>I1-H2</i>	2.57	3.28
<i>I1-H3</i>	3.73	3.00
<i>I1-H4</i>	2.95	3.69
<i>I1-H5</i>	2.57	2.56
<i>I2-H1</i>	3.97, 3.86	3.45
<i>I2-H2</i>	3.32, 3.97	3.82
<i>I2-H3</i>	3.32	3.06
<i>I2-H4</i>	4.26, 3.73	3.11
<i>I2-H5</i>	2.57	3.11
<i>I3-H1</i>	3.33	3.84, 3.94
<i>I3-H2</i>	4.94	2.58
<i>I3-H3</i>	3.19	3.83
<i>I3-H4</i>	3.20	2.97
<i>I3-H5</i>	3.91	3.31

REFERENCES

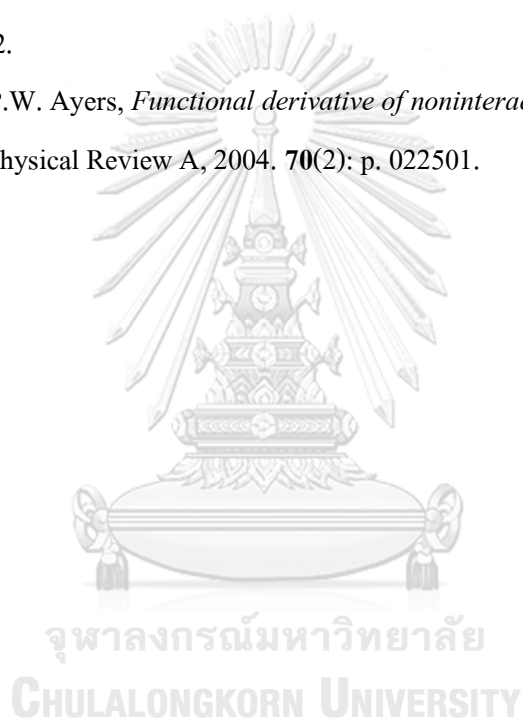
1. Zhou, H., et al., *Interface engineering of highly efficient perovskite solar cells*. 2014. **345**(6196): p. 542-546.
2. Green, M.A., A. Ho-Baillie, and H.J. Snaith, *The emergence of perovskite solar cells*. Nature Photonics, 2014. **8**: p. 506.
3. M. Brenner, T., et al., *Hybrid Organic-Inorganic Perovskites: Low-Cost Semiconductors with Intriguing Charge-Transport Properties*. Vol. 1. 2016. 15007.
4. Miyano, K., et al., *Hysteresis, stability, and ion migration in lead halide perovskite photovoltaics*. The journal of physical chemistry letters, 2016. **7**(12): p. 2240-2245.
5. Weber, D., *CH₃NH₃PbX₃, ein Pb(II)-System mit kubischer Perowskitstruktur / CH₃NH₃PbX₃, a Pb(II)-System with Cubic Perovskite Structure*. Vol. 33. 1978.
6. Mitzi, D.B., et al., *Conducting tin halides with a layered organic-based perovskite structure*. Nature, 1994. **369**(6480): p. 467.
7. Mitzi, D., et al., *Conducting layered organic-inorganic halides containing < 110 >-oriented perovskite sheets*. Science, 1995. **267**(5203): p. 1473-1476.
8. Mitzi, D.B., et al., *Transport, optical, and magnetic properties of the conducting halide perovskite CH₃NH₃SnI₃*. Journal of Solid State Chemistry, 1995. **114**(1): p. 159-163.
9. Mitzi, D.B., *Synthesis, structure, and properties of organic -inorganic perovskites and related materials*. Progress in inorganic chemistry, 1999: p. 1-121.
10. Kojima, A., et al., *Organometal halide perovskites as visible-light sensitizers for photovoltaic cells*. Journal of the American Chemical Society, 2009. **131**(17): p. 6050-6051.
11. Brittman, S., G.W.P. Adhyaksa, and E.C. Garnett, *The expanding world of hybrid perovskites: materials properties and emerging applications*. MRS communications, 2015. **5**(1): p. 7-26.
12. Stranks, S.D. and H.J. Snaith, *Metal-halide perovskites for photovoltaic and light-emitting devices*. Nature nanotechnology, 2015. **10**(5): p. 391.
13. Bryant, D., et al., *Light and oxygen induced degradation limits the operational stability of methylammonium lead triiodide perovskite solar cells*. Energy & Environmental Science, 2016. **9**(5): p. 1655-1660.

14. Frost, J.M., et al., *Atomistic origins of high-performance in hybrid halide perovskite solar cells*. Nano letters, 2014. **14**(5): p. 2584-2590.
15. Weller, M.T., et al., *Complete structure and cation orientation in the perovskite photovoltaic methylammonium lead iodide between 100 and 352 K*. Chemical Communications, 2015. **51**(20): p. 4180-4183.
16. Yang, W.S., et al., *High-performance photovoltaic perovskite layers fabricated through intramolecular exchange*. 2015. **348**(6240): p. 1234-1237.
17. Amat, A., et al., *Cation-Induced Band-Gap Tuning in Organohalide Perovskites: Interplay of Spin–Orbit Coupling and Octahedra Tilting*. Nano Letters, 2014. **14**(6): p. 3608-3616.
18. Stoumpos, C.C., C.D. Malliakas, and M.G. Kanatzidis, *Semiconducting tin and lead iodide perovskites with organic cations: phase transitions, high mobilities, and near-infrared photoluminescent properties*. Inorganic chemistry, 2013. **52**(15): p. 9019-9038.
19. Weller, M.T., et al., *Cubic Perovskite Structure of Black Formamidinium Lead Iodide, α -[HC(NH₂)₂]PbI₃, at 298 K*. The Journal of Physical Chemistry Letters, 2015. **6**(16): p. 3209-3212.
20. Chen, T., et al., *Entropy-driven structural transition and kinetic trapping in formamidinium lead iodide perovskite*. Science advances, 2016. **2**(10): p. e1601650-e1601650.
21. Motta, C., et al., *Revealing the role of organic cations in hybrid halide perovskite CH₃NH₃PbI₃*. Nature communications, 2015. **6**: p. 7026.
22. Lahnsteiner, J., et al., *Room-temperature dynamic correlation between methylammonium molecules in lead-iodine based perovskites: An ab initio molecular dynamics perspective*. Physical Review B, 2016. **94**(21): p. 214114.
23. Klinkla, R., et al., *The crucial role of density functional nonlocality and on-axis CH₃NH₃ rotation induced I₂ formation in hybrid organic-inorganic CH₃NH₃PbI₃ cubic perovskite*. Scientific Reports, 2018. **8**(1): p. 13161.
24. Brivio, F., et al., *Relativistic quasiparticle self-consistent electronic structure of hybrid halide perovskite photovoltaic absorbers*. Physical Review B, 2014. **89**(15): p. 155204.
25. Hohenberg, P. and W. Kohn, *Inhomogeneous Electron Gas*. Physical Review, 1964. **136**(3B): p. B864-B871.
26. Born, M. and R. Oppenheimer, *Zur Quantentheorie der Molekeln*. Annalen der Physik,

1927. **389**(20): p. 457-484.
27. Hartree, D.R. *The wave mechanics of an atom with a non-coulomb central field. Part II. Some results and discussion.* in *Mathematical Proceedings of the Cambridge Philosophical Society*. 1928. Cambridge University Press.
28. Fock, V., *Näherungsmethode zur Lösung des quantenmechanischen Mehrkörperproblems.* Zeitschrift für Physik, 1930. **61**(1-2): p. 126-148.
29. Kohn, W. and L.J. Sham, *Self-consistent equations including exchange and correlation effects.* Physical review, 1965. **140**(4A): p. A1133.
30. Perdew, J.P. and Y. Wang, *Accurate and simple analytic representation of the electron-gas correlation energy.* Physical Review B, 1992. **45**(23): p. 13244.
31. Ceperley, D.M. and B. Alder, *Ground state of the electron gas by a stochastic method.* Physical Review Letters, 1980. **45**(7): p. 566.
32. Bloch, F., *Über die quantenmechanik der elektronen in kristallgittern.* Zeitschrift für physik, 1929. **52**(7-8): p. 555-600.
33. Blöchl, P.E., *Projector augmented-wave method.* Physical Review B, 1994. **50**(24): p. 17953-17979.
34. Li, J. and I. Yip, *Handbook of Materials Modeling.* Yip. Chapter 2.8 Basic Molecular Dynamics, 2005: p. 565-588.
35. Monkhorst, H.J. and J.D. Pack, *Special points for Brillouin-zone integrations.* Physical review B, 1976. **13**(12): p. 5188.
36. Pfrommer, B.G., et al., *Relaxation of crystals with the quasi-Newton method.* Journal of Computational Physics, 1997. **131**(1): p. 233-240.
37. Head, J.D. and M.C. Zerner, *A Broyden—Fletcher—Goldfarb—Shanno optimization procedure for molecular geometries.* Chemical physics letters, 1985. **122**(3): p. 264-270.
38. Thomas, L.H., *The motion of the spinning electron.* Nature, 1926. **117**(2945): p. 514.
39. Navrotsky, A., *Energetics and crystal chemical systematics among ilmenite, lithium niobate, and perovskite structures.* Chemistry of Materials, 1998. **10**(10): p. 2787-2793.
40. Giannozzi, P., et al., *QUANTUM ESPRESSO: a modular and open-source software project for quantum simulations of materials.* Journal of physics: Condensed matter, 2009. **21**(39): p. 395502.

41. Hobbs, D., G. Kresse, and J. Hafner, *Fully unconstrained noncollinear magnetism within the projector augmented-wave method*. Physical Review B, 2000. **62**(17): p. 11556.
42. Perdew, J.P., K. Burke, and M. Ernzerhof, *Generalized Gradient Approximation Made Simple*. Physical Review Letters, 1996. **77**(18): p. 3865-3868.
43. Anderson, J. and A. Gold, *Fermi surface, pseudopotential coefficients, and spin-orbit coupling in lead*. Physical Review, 1965. **139**(5A): p. A1459.
44. Corso, A.D. and A.M. Conte, *Spin-orbit coupling with ultrasoft pseudopotentials: Application to Au and Pt*. Physical Review B, 2005. **71**(11): p. 115106.
45. Stroppa, A., et al., *Tunable ferroelectric polarization and its interplay with spin-orbit coupling in tin iodide perovskites*. Nature Communications, 2014. **5**: p. 5900.
46. Goldstein, H., C. Poole, and J. Safko, *Classical mechanics*. 3rd. 2002, Addison Wesley.
47. Renka, R.J., R. Renka, and A. CLINE, *A triangle-based C^1 interpolation method*. The Rocky Mountain journal of mathematics, 1984: p. 223-237.
48. Fabini, D.H., et al., *Universal dynamics of molecular reorientation in hybrid lead iodide perovskites*. Journal of the American Chemical Society, 2017. **139**(46): p. 16875-16884.
49. Hansen, J.P. and I.R. McDonald, *Theory of simple liquids*. Physics Today, 1988. **41**: p. 89.
50. Lee, J.-H., et al., *Resolving the physical origin of octahedral tilting in halide perovskites*. Chemistry of Materials, 2016. **28**(12): p. 4259-4266.
51. McKechnie, S., et al., *Dynamic symmetry breaking and spin splitting in metal halide perovskites*. Physical Review B, 2018. **98**(8): p. 085108.
52. Mosconi, E., et al., *First-principles modeling of mixed halide organometal perovskites for photovoltaic applications*. The Journal of Physical Chemistry C, 2013. **117**(27): p. 13902-13913.
53. Tao, S.X., X. Cao, and P.A. Bobbert, *Accurate and efficient band gap predictions of metal halide perovskites using the DFT-1/2 method: GW accuracy with DFT expense*. Scientific reports, 2017. **7**(1): p. 14386.
54. Filip, M.R. and F. Giustino, *G W quasiparticle band gap of the hybrid organic-inorganic perovskite $\text{CH}_3\text{NH}_3\text{PbI}_3$: Effect of spin-orbit interaction, semicore electrons, and self-consistency*. Physical Review B, 2014. **90**(24): p. 245145.
55. Hernández-Haro, N., et al., *DFT prediction of band gap in organic-inorganic metal halide*

- perovskites: An exchange-correlation functional benchmark study*. Chemical Physics, 2019. **516**: p. 225-231.
56. Perdew, J.P., et al., *Understanding band gaps of solids in generalized Kohn–Sham theory*. Proceedings of the National Academy of Sciences, 2017. **114**(11): p. 2801-2806.
57. Kim, M., et al., *Switchable $S = 1/2$ and $J = 1/2$ Rashba bands in ferroelectric halide perovskites*. 2014. **111**(19): p. 6900-6904.
58. Mosconi, E., T. Etienne, and F. De Angelis, *Rashba band splitting in organohalide lead perovskites: bulk and surface effects*. The journal of physical chemistry letters, 2017. **8**(10): p. 2247-2252.
59. Liu, S. and P.W. Ayers, *Functional derivative of noninteracting kinetic energy density functional*. Physical Review A, 2004. **70**(2): p. 022501.



VITA

NAME Wiwittawin Sukmas

DATE OF BIRTH 6 October 1994

PLACE OF BIRTH Bangkok, Thailand

INSTITUTIONS ATTENDED Chulalongkorn University

HOME ADDRESS 6/6 moo 2 Samrongklang Prapadaeng Samutprakarn

PUBLICATION Organic Molecule Orientations and Rashba-Dresselhaus Effect in α -Formamidineum Lead Iodide
Wiwittawin Sukmas, Udomsilp Pinsook, Prutthipong
Tsuppayakorn-aeck, Teerachote Pakornchote, Akkarach Sukserm,
and Thiti Bovornratanaraks
The Journal of Physical Chemistry C Just Accepted Manuscript
DOI: 10.1021/acs.jpcc.9b02140